# DIFFERENTIAL LIGHT SCATTERING SPECTROSCOPY MEASUREMENTS FOR DETECTING AND IMAGING CANCER

BY

CONDON LAU

B.S.E. Mechanical and Aerospace Engineering
Princeton University, 2004

Submitted to the Department of Mechanical Engineering in partial fulfillment of the requirements for the Degree of Master of Science in Mechanical Engineering.

MASSACHUSETTS INSTITUTE OF TECHNOLOGY

January, 2006

© 2006 Massachusetts Institute of Technology
All rights reserved

Signature of Author: _____
Department of Mechanical Engineering
February 03, 2006

Certified by: _____
Michael Feld
Professor of Physics

_____
Peter So
Professor of Mechanical Engineering

Accepted by: _____
Lallit Anand
Professor of Mechanical Engineering
Graduate Officer

MASSACHUSETTS INSTITUTE OF TECHNOLOGY
JUL 14 2006
LIBRARIES

BARKER

## Abstract

Optical spectroscopy show great promise for diagnosing the earliest stages of cancer. Light scattering spectroscopy (LSS), the study of single elastic backscattering as a function of wavelength and angle, can detect subcellular structural changes in early cancer. We have developed two novel differential light scattering spectroscopy techniques, space differential LSS (SD/LSS) and $\phi$-angle differential LSS ($\phi$/LSS), for detecting the single backscattering signal from a reflectance spectrum dominated by multiple scattering and diffuse reflectance. SD/LSS exploits the penetration abilities of diffuse reflectance while $\phi$/LSS exploits the angular asymmetry of single backscattering from large particles. $\phi$/LSS has the added advantage of being able to isolate single backscattering specifically from scatterers much larger than the wavelength. We implement $\phi$/LSS to interrogate colon tissue and to develop diagnostic algorithms based on Mie theory. The results show great promise for diagnosing cancer. Instrumentation is being developed to implement SD/LSS and $\phi$/LSS together in a wide area imaging system with the goal of studying and detecting cancer at its earliest stages *in vivo* and in real time. The system has been validated with controlled tissue phantoms and will soon be ready for clinical studies.

## Table of Contents


Introduction ..... 3

1. Spectroscopic techniques for cancer diagnosis ..... 12
   1.1. Spectroscopy for cancer detection ..... 12
   1.2. Spectroscopic imaging ..... 17

2. Principles of light scattering in tissue ..... 23
   2.1. Two-layer tissue model ..... 23
   2.2. Principles of light scattering from a single particle ..... 24
   2.3. Scattering by particles smaller than the wavelength ..... 29
   2.4. Scattering by a homogeneous sphere of arbitrary size ..... 31
   2.5. Scattering by a tissue-like collection of non-ideal particles ..... 35

3. Techniques for isolating single backscattering ..... 41
   3.1. LSS research ..... 41
   3.2. Space differential LSS ..... 44
   3.3. $\phi$-angle differential LSS ..... 46
   3.4. Differential LSS imaging ..... 48

4. Implementation and experimental results ..... 52
   4.1. $\phi$/LSS on tissue phantoms ..... 52
   4.2. $\phi$/LSS on *ex vivo* colon tissue ..... 65
   4.3. SD/LSS effectiveness ..... 74
   4.4. Spectroscopic imaging with SD/LSS and $\phi$/LSS ..... 76

Conclusion ..... 81

Appendix A. Mie fitting program for $\phi$/LSS *ex vivo* tissue study ..... 84

Appendix B. Signal to noise analysis ..... 88

Appendix C. Measuring scattering at select $\theta$ and $\phi$ ..... 90

## Introduction

Cancer is the second leading cause of death in the world. Each year, cancer kills over 500 thousand people in the United States alone[1]. The vast majority of human cancers originate in the epithelium of the body cavities, including the gastrointestinal, respiratory, and genitourinary systems[2]. The epithelium is the outermost protective layer of cells lining the body's surfaces. In open cavities such as the mouth and cervix, the epithelium is exposed to air while in organs such as the stomach, the epithelium is in contact with digestive juices. Virtually all epithelial cancers are treatable if detected at an early, pre-invasive stage. If the cancer is allowed to metastasize, treatment becomes much more difficult. Current cancer diagnosis methods usually involve two medical procedures. The first procedure is a wide-area surveillance over the tissue, such as mammography, colposcopy, palpation (examination by touch), or visual examination. When warning signs are present, small pieces of tissue from suspicious sites are excised from the patient and the cellular morphology is analyzed under a microscope. This second procedure is called biopsy and is the gold standard of cancer diagnosis. Unfortunately, many forms of precancerous and early cancerous lesions are difficult to detect using traditional surveillance procedures. The current wide-area surveillance methods lack sensitivity and biopsies can only sample a small portion of the at risk tissue. Therefore, there is a need for wide-area imaging systems capable of detecting cancer in its earliest stages.

So far, the majority of imaging modalities focus on tissue structure or anatomy at the organ scale, which is not sufficient for detecting tiny precancers at their earliest stages[3]. Biochemical and subcellular morphological changes have been shown to

accompany cancer development[4]. Some of the most prominent changes are enlargement, crowding, and darkening of nuclei in cancerous epithelial cells. Nuclei are typically 4 - 7μm in size, but can expand to the volume of the cell in cancerous cells[5]. We focus on nuclear changes in this thesis. It will be most beneficial to develop new cancer imaging modalities that provide subcellular biochemical and morphological information. Several new optical imaging modalities target these features and recent testing has shown great promise. These modalities illuminate the tissue surface with light and collect the returning light for analysis.

**Confocal microscopy imaging**: Confocal microscopy uses a pinhole to selectively focus light from a small area (several microns) of the tissue. The pinhole is "scanned" across the tissue surface. The images produced are due to light scattered backwards at interfaces of different refractive index. The confocal setup prevents light scattered from outside the region of interest from being focused on the camera, producing thin section images with high resolution and contrast. The size of the pinhole, among other variables, determines the depth and lateral resolution of the system. Several research groups have demonstrated the use of confocal scanning microscopes for imaging human and animal tissues, both *ex vivo* and *in vivo*[6]. Skin and oral mucosa are easily accessible with this technique. The technique has also been applied to image bladder[7], embryo[8] [9], kidney[10], skin[11], and retina[12].

**Optical coherence tomography**: Optical coherence tomography (OCT) utilizes the coherence properties of light to obtain cross sectional images of scattering media such as living tissue[13]. This technique employs low coherence light (light with a short coherence length) in a Michelson interferometer. The specimen is placed at the end of the sample

arm. Backscattered light interferes with light returning from the mirror in the reference arm. Constructive interference occurs only when the distance to a scattering interface in the sample matches that to the reference mirror to within the coherence length. Depth is probed by scanning the reference mirror position and detecting the interference signal. Cross-sectional images can be built up from multiple axial scans at different transverse positions in the sample. As with confocal microscopy, image formation is again due to refractive index change. In turbid tissues, imaging depths on the order of one millimeter can be achieved, with resolution on the order of several tens of microns. OCT has been used to obtain *in vivo* images of clear tissues such as the human eye[14] and turbid tissues such as esophageal mucosa[15]. It has also been used to image intra-arterial walls, arthritic cartilage and gynecologic neoplasms, and *in vitro* frog embryos[16 17 18].

**Polarization imaging**: Several groups have used polarized light to image superficial tissues. Linearly polarized light illuminates the tissue surface. If scattered light with the same polarization is collected, superficial features are observed. If the opposite polarization is collected, sub-surface features are observed[19]. Anderson et al.[20] used polarized light to enhance contrast in skin images by separating the specularly reflected and multiply-scattered components of light emerging from skin. Jacques et al. used polarized light to image superficial layers of human skin[21].

**Fluorescence imaging**: Fluorescence is induced by the excitation of fluorophores in the tissue, usually with deep blue or ultraviolet illumination. Therefore, fluorescence contains information about fluorophore concentrations in the tissue. This provides valuable biochemical information. Two-photon microscopy is capable of imaging fluorophores deep within a tissue sample[22]. Fluorescent dyes introduced to the patient mark target

structures in the tissue. Wu et. al. have measured tissue auto-fluorescence, fluorescence from native fluorophores, to detect neoplastic growths *in vivo*[23]. Wang et. al. have also developed a fluorescence imaging system for *in vivo* identification of colonic dysplasia[24]. This project has been translated into Pentax's recently released Lung cancer imaging system, the Safe 3000.

The imaging modalities above use all of the returned light to form an image. In the cases of confocal microscopy, OCT, and polarization imaging, the light is focused on the camera to form a physical image of the cellular morphology. Fluorescence imaging maps fluorescence intensity from different positions of the tissue. These techniques have provided good results for cancer diagnosis, but we can gain extra diagnostic power by distinguishing the returned light by color. The technique of studying the frequency/wavelength spectrum of returned light is called Spectroscopy. It has been used extensively to identify unknown substances. Spectroscopy is not restricted to using electromagnetic waves near the visible regime (400nm to 700nm); other spectroscopic concepts such as neutron scattering spectroscopy provide valuable information on the properties of matter[25]. In this thesis we will focus on spectroscopy with visible and near-visible light for diagnosis of precancer.

Spectroscopy has recently proven to be a powerful diagnostic tool for many types of precancer[26] [27]. In medical spectroscopy, light photons excite (illuminate) the tissue surface and emitted (returning) photons are measured at each wavelength. Several of the exciting new spectroscopic modalities are elastic light scattering (ELSS), absorption (AS),

fluorescence (FS), and Raman spectroscopy (RS). ELSS utilizes light scattered at the same wavelength as the incident light. AS uses the spectrum of scattered light to determine the energy absorption properties of the tissue. FS uses the spectrum of fluorescence and RS uses the Raman effect[28]. Spectroscopy can provide structural and biochemical information at the subcellular level[29]. The fundamentals of these modalities along with the latest medically relevant research will be reviewed in detail in chapter 1. To date, the use of spectroscopy for cancer diagnosis has primarily focused on diagnosis of small tissue areas on the order of several square millimeters. One average diagnosis is given for the area. Spectroscopic diagnosis can be conducted by using an optical fiber probe that delivers excitation light to the tissue surface and collects returned light.

Being able to perform spectroscopic diagnosis over a wide area of several $cm^2$ is a potentially very powerful surveillance technique. Spectroscopic imaging illuminates a wide area of tissue with light and collects the spectra of light returned from each region in the area. The spectra are analyzed to provide cancer diagnosis in each region. Conducting spectroscopic diagnosis over a wide area greatly reduces the risk of missing small cancerous growth. It can also be used to assess cancer margins, such as in breast, to insure tumors have been completely removed during surgery. Ultimately, spectroscopic imaging can serve as a guide to biopsy to avoid unnecessary excisions and greatly reduce medical costs. If the techniques prove sufficiently accurate, they may replace biopsy as the gold standard of cancer diagnosis. Spectroscopic imaging can be implemented through common medical devices such as colposcopes (cervix) and imaging endoscopes.

Research on spectroscopic imaging has been in progress for several years. Benavides et. al developed a colposcope capable of conducting FS and ELSS over a 3.5cm diameter area of the cervix[30]. Gurjar et. al. of the MIT Spectroscopy Laboratory implemented a special case of ELSS, which considered only photons that singly backscattered from the tissue (LSS), over a $1.7cm^2$ square area of *ex vivo* colon tissue divided into over ten thousand 125μm by 125μm regions[31]. A detailed review of current advances in spectroscopic imaging is in chapter 1. The research to be presented in this thesis springs from the work of Gurjar et. al.

This thesis is the basic studies part of a project to develop spectroscopic imaging systems based on ELSS, AS, and FS for cancer diagnosis in cervix and oral cavity. We have developed two novel techniques based on the difference between two ELSS signals to conduct spectroscopic imaging. The goal of this thesis is to evaluate the potential of these techniques for measuring cellular morphology and diagnosing cancer with tissue phantom and *ex vivo* tissue experiments. We also develop a physical model based on light scattering theory to understand the origins of the measured spectra and to extract scatterer properties. Testing is conducted with instrumentation that can be transferred to the clinical imaging system. Chapter 1 provides fundamental concepts and recent research on frequently used spectroscopic modalities for cancer detection. Chapter 2 reviews the fundamental physics of elastic light scattering relevant to elastic light scattering spectroscopy. Chapter 3 samples previous research on LSS for cancer detection and explores challenges involved with implementing LSS. This chapter also presents our two novel differential measurements and how they address the challenges presented by LSS

while improving spectroscopic imaging using LSS. Chapter 4 presents instrumentation and experimental results and discusses findings from tissue phantom and *ex vivo* tissue studies.

---

[1] H. Weir, M. Thun, B. Hankey, L. Ries, H. Howe, P. Wingo, A. Jemal, E. Ward, R. Anderson, B. Edwards; "Annual Report to the Nation on the Status of Cancer, 1975-2000, Featuring the Uses of Surveillance Data for Cancer Prevention and Control"; J. of the National Cancer Inst.; Vol. 95, 1276-1299 (2003).

[2] A. Jemal, T. Murray, E. Ward, A. Samuels, R. Tiwari, A. Ghafoor, E. Feuer, and M. Thun; "Cancer statistics, 2005"; CA Cancer J Clin; Vol. 55, 10-30 (2005).

[3] D. Benaron; "The future of cancer imaging"; Cancer and Metastasis Reviews; Vol. 21, 45-78 (2002).

[4] R. Cotran, V. Kumar, T. Collins; Pathologic Basis of Disease; W.B. Saunders Company (1999).

[5] L. Perelman, V. Backman, G. Zonios, R. Manoharan, A. Nusrat, S. Shields, M. Seiler, C. Lima, T. Hamano, I. Itzkan, J. Van Dam, J. Crawford, M. Feld; "Observation of Periodic Fine Structure in Reflectance from Biological Tissue: A New Technique for Measuring Nuclear Size Distribution", Physical Review Letters; Vol. 80, No. 3, 627-30 (1998).

[6] W. Petroll, H. Cavanagh, J. Jester; "Clinical confocal microscopy"; Curr. Opin. Ophthalmol.; Vol. 9, 59-65 (1998).

[7] F. Koenig, S. Gonzalez, W. White, M. Lein, M. Rajadhyaksha; "Near-infrared confocal laser scanning microscopy of bladder tissue in vivo"; *Urology*; Vol. 53, 853-857 (1999).

[8] P. Kulesa, S. Fraser; "Confocal imaging of living cells in intact embryos"; Methods Mol. Biol; Vol. 122, 205-222 (1999).

[9] S. Gonzalez, M. Rajadhyaksha, A. Gonzalez-Serva, W. White, R. Anderson; "Confocal reflectance imaging of folliculitis in vivo: correlation with routine histology"; J. Cutan. Pathol.; Vol. 26, 201-5 (1999).

[10] M. Kneen, D. Harkin, L. Walker, D. Alcorn, P. Harris; "Imaging of renal medullary interstitial cells in situ by confocal fluorescence microscopy"; Anat. Embryol.; Vol. 200, 117-21 (1999).

[11] M. Rajadhyaksha, R. Anderson, R. Webb; "Video-rate confocal scanning laser microscope for imaging human tissues in vivo"; Appl. Opt.; Vol. 38 (1999).

[12] P. Vieira, A. Manivannan, C. Lim, P. Sharp, J. Forrester; "Tomographic reconstruction of the retina using a confocal scanning laser ophthalmoscope"; Physiol. Meas.; Vol. 20, 1-19 (1999).

[13] D. Huang, E. Swanson, C. Lin, J. Schuman, W. Stinson, W. Chang, M. Hee, T. Flotte, K. Gregory, C. Puliafito, J. Fujimoto; "Optical coherence tomography"; Science; Vol. 254, 1178-1181 (1991).

[14] M. Hee, J. Izatt, E. Swanson, D. Huang, J. Schuman, C. Lin, C. Puliafito, J. Fujimoto; "Optical coherence tomography of the human retina"; Arch. Ophthalmol.; Vol. 113, 325-32 (1995).

[15] K. Kobayashi, J. Izatt, M. Kulkarni, J. Willis, M. Sivak; "High-resolution cross-sectional imaging of the gastrointestinal tract using optical coherence tomography: preliminary results"; Gastrointest. Endosc.; Vol. 47, 515-23 (1998).

[16] J. Fujimoto, S. Boppart, G. Tearney, B. Bouma, C. Pitris, M. Brezinski; "High resolution in vivo intra-arterial imaging with optical coherence tomography"; Heart; Vol. 82, 128-133 (1999).

[17] S. Boppart, B. Bouma, C. Pitris, J. Southern, M. Brezinski, J. Fujimoto; "In vivo cellular optical coherence tomography imaging"; Nature Medicine; Vol. 4, 861-5 (1998).

[18] C. Pitris, A. Goodman, S. Boppart, J. Libus, J. Fujimoto, M. Brezinski; "High-resolution imaging of gynecologic neoplasms using optical coherence tomography"; Obstet. Gynecol.; Vol. 93, 135-139 (1999).

[19] S. Demos, R. Alfano; "Optical polarized imaging"; App. Opt.; Vol. 36, 150-155 (1997).

[20] R. Anderson; "Polarized light examination and photography of the skin"; Arch. Dermatol.; Vol. 127, 1000-1005 (1991).

[21] S. Jacques, J. Roman, K. Lee; "Imaging Superficial Tissues with Polarized Light"; Las. Surg. Med.; Vol. 26, 119-129 (2000).

[22] W. Denk, J. Strickler, W. Webb; "Two-photon laser scanning fluorescence microscopy"; Science; Vol. 248, 73-76 (1990).

[23] T. Wu, J. Qu, T. Cheung, K. Lo, M. Yu; "Preliminary study of detecting neoplastic growths in vivo with real time calibrated autofluorescence imaging"; Optics Express; Vol. 11, No. 4 (2003).

[24] T. Wang, J. Crawford, M. Feld, Y. Wang, I. Itzkan, J. Van Dam; "In vivo identification of colonic dysplasia using fluorescence endoscopic imaging"; Gastrointestinal Endoscopy; Vol. 49, 447-455 (1999).

[25] P. Mitchell, S. Parker, A. Ramirez-Cuesta, J. Tomkinson; Vibrational Spectroscopy with Neutrons; World Scientific (2005).

[26] V. Backman, M. Wallace, L. Perelman, J. Arendt, R. Gurjar, M. Müller, Q. Zhang, G. Zonios, E. Kline, T. McGillican, S. Shapshay, T. Valdez, K. Badizadegan, J. Crawford, M. Fitzmaurice, S. Kabani, H. Levin, M. Seiler, R. Dasari, I. Itzkan, J. Van Dam, M. Feld; "Detection of Preinvasive Cancer Cells"; Nature; Vol. 406, 35-6 (2000).

[27] Y. Mirabal, S. Chang, E. Atkinson, A. Malpica, M. Follen, R. Richards-Kortum; "Reflectance Spectroscopy for *in-vivo* detection of cervical precancer"; J. Biomedical Optics; Vol. 7, 587-94 (2002).

[28] C. Raman, K. Krishnan; "A New Type of Secondary Radiation"; Nature; Vol. 121 (1928).

[29] G. Zonios, L. Perelman, V. Backman, R. Manoharan, M. Fitzmaurice, J. Van Dam, M. Feld; "Diffuse reflectance spectroscopy of human adenomatous colon polyps *in vivo*"; Applied Optics, Vol. 38, No. 31, 6628-37 (1999).

[30] J. Benavides, S. Chang, S. Park, R. Richards-Kortum, N. Mackinnon, C. MacAulay, A. Milbourne, A. Malpica, M. Follen; "Multispectral digital colposcopy for *in vivo* detection of cervical cancer"; Optics Express; Vol. 11, No. 10, 1223-36 (2003).

[31] R. Gurjar, V. Backman, L. Perelman, I. Georgakoudi, K. Badizadegan, I. Itzkan, R. Dasari, M. Feld; "Imaging human epithelial properties with polarized light-scattering spectroscopy"; Nature Medicine; Vol. 7, 1245-8 (2001).

# Chapter 1:

# Spectroscopic techniques for cancer diagnosis

Spectroscopy excites the sample with light and the emitted light can be analyzed by wavelength. Depending on the type of spectroscopy, the illumination light can be monochromatic or broadband and is typically provided by a laser or a white light source. Also, a diffraction grating may be used to disperse the emitted light into its different colors. Spectroscopy has been used extensively to identify unknown substances. In medicine, spectroscopy can provide information about tissue structure and biochemistry not accessible to conventional screening methods. This chapter reviews the literature on spectroscopy for cancer detection. Section 1.1 reviews spectroscopic modalities applied over small areas of tissue. Section 1.2 reviews previous research on spectroscopic imaging, one of the focuses of this thesis.

## 1.1 Spectroscopy for cancer detection

Much progress has been made in applying conventional spectroscopic modalities to cancer detection. This section reviews 3 frequenctly used modalities: Raman spectroscopy (RS), fluorescence spectroscopy (FS), and reflectance spectroscopy (RES). The accuracy of diagnosis is compared to biopsy and expert analysis by a pathologist. Accuracy is described by sensitivity (percentage of samples correctly diagnosed as diseased) and specificity (percentage of samples correctly diagnosed as healthy).

**Raman spectroscopy**: Raman spectroscopy (RS) relies on the Raman effect, first observed by Raman and Krishnan[1]. Photons at a given wavelength incident on a molecule are inelastically scattered such that the scattered light occurs in a pattern of spectral lines shifted in wavelength from the incident light. Two shifts, one to shorter wavelengths (anti-Stokes) and the other to longer wavelengths (Stokes), are observed. The Stokes scatter has higher intensity and is usually the one observed with near-visible infrared excitation wavelengths. The shift in spectral line pattern is molecule specific. Raman scattering is typically much weaker then elastic scattering (not shifted in wavelength), but narrow bandwidth lasers can provide sufficient excitation intensity to overcome noise. Therefore, Raman spectroscopy has been very valuable for identifying chemical constituents. Since cancer progression is accompanied by biochemical changes in the epithelium, RS can potentially track the changes and diagnose cancer[2]. Utzinger et. al conducted RS *in vivo* to detect squamous dysplasia, a precursor to cervical cancer[3]. They illuminated a 12mm diameter of cervix with 789nm laser excitation and measured the spatially averaged Raman scatter. From 24 measurements done on 13 patients, they observed peaks at 1070, 1180, 1195, 1210, 1245, 1330, 1400, 1454, 1505, 1555, 1656, and 1760 $cm^{-1}$. Biopsies were independently analyzed from the measured regions. The researchers found a large intensity ratio $I(\lambda = 1454) / I(\lambda = 1656)$ and a small ratio $I(\lambda = 1330) / I(\lambda = 1454)$ correctly distinguished squamous dysplasia from other tissue types in all but one case. Kendall et. al applied Raman spectroscopy to classifying neoplasia (abnormal cell growth) in Barrett's oesophagus *ex vivo*[4]. Eighty-seven samples were excised from 44 patients and independently classified by three pathologists. They obtained sensitivities from 73% to 100% and specificities from 90% to 100%, depending

on the tissue state distinction (eg. Barrett's vs. neoplastic) targeted. Haka et. al used RS to identify benign and malignant lesions in breast tissue *ex vivo*[5]. They also developed a model using basis Raman spectra from nine morphological and chemical features of breast tissue. The measured spectra were fitted to these basis spectra to extract the morphological and chemical makeup of the tissue. From the spectroscopically measured content of fat and collagen, the researchers obtained 94% sensitivity and 96% specificity distinguishing malignant tissue from other types. Raman spectroscopy offers great potential for precancer diagnosis.

**Fluorescence spectroscopy**: Fluorescence spectroscopy (FS) exploits the variety in absorption and emission properties of molecules. In fluorescence, light at a certain wavelength excites a molecule and light at longer wavelengths is emitted[6]. For each excitation wavelength there is an emission spectrum. Similar to Raman spectroscopy, each excitation-emission spectrum carries molecule specific information, so FS can be used to track biochemical changes in cancer progression. Typically, the excitation light is low intensity UV radiation and the emission wavelengths are visible. This is convenient for data acquisition because most optics and CCD cameras are designed for visible light. FS can be conducted with fluorescence stains that bond with certain molecules. In this thesis, we focus on autofluorescence, which is fluorescence from native tissue molecules. Ramanujam et. al. excited cervix with 380nm and 460nm light and measured the emission spectra[7]. With the 460nm spectra, they were able to differentiate squamous intraepithelial lesions (SIL) from normal squamous tissue with 91% sensitivity and 75.5% specificity. They were also able to differentiate high-grade SILs from low-grade SILs with 80% sensitivity and 76% specificity. With 360nm spectra, SILs were

distinguished from inflammation and normal columnar tissue with 77% sensitivity and 72% specificity. Wang et. al. studied fluorescence spectra from *ex vivo* oral tissue using one and two wavelength excitation[8]. They found exciting with two wavelengths simultaneously gave 81% sensitivity and 94% specificity when separating healthy from cancerous tissue. Bard et. al. combine FS with RES (discussed below) to detect carcinoma (CIS) and dysplastic lesions in the bronchial tree *in vitro*[9]. *In vivo* measurements on 21 patients found combining FS with RES distinguished high-grade lesions from low-grade lesions with specificity improved from using fluorescence alone. Fluorescence spectroscopy has great potential for detecting biochemical changes in cancer progression.

**Reflectance spectroscopy**: Reflectance spectroscopy (RES) utilizes spectral changes in elastic scattering and absorption. Elastic scattering is the dominant form of light scattering and depends on scatterer structure. Light at some wavelength exciting a particle is emitted at the same wavelength, as opposed to Raman scattering and fluorescence. Absorption occurs when a photon is not emitted after excitation. The incident energy has been transformed to a non-electromagnetic form. The total emitted spectrum (reflectance spectrum) will be a combination of the effects of scattering and absorption. RES combines elastic light scattering spectroscopy and absorption spectroscopy. In this thesis, we distinguish between two types of reflectance spectroscopy: diffuse reflectance (DRS) and light scattering spectroscopy (LSS). DRS measures light that has undergone multiple scattering events in the tissue. The returned diffuse light has a Lambertian profile, where the intensity at an angle $\theta$ from the direction of maximum intensity, $I_0$, is $I_0 * \cos\theta$. DRS with near-visible wavelength excitation can penetrate

beyond the first layer of cells and assess scatterer and absorber concentrations. Scattering and absorption at these wavelengths provide information on tissue structure and hemoglobin (Hb) concentration, respectively[10]. In human tissue, diffuse reflectance dominates the total reflectance spectrum, thus when authors refer to reflectance, they are usually studying diffuse reflectance. LSS analyzes light that has scattered only once (single backscattering) before returning from the tissue. LSS provides information on the most superficial epithelial cells[11]. Because LSS relies on single scattering, it is able to measure detailed scattering properties of cells and thus, their subcellular morphology[12]. Light scattering theory and LSS research is reviewed in chapter 2. Zonios et. al. used DRS to measure scatterer and absorber concentrations in colon polyps *in vivo*. They fitted measured reflectance spectra to a diffusion limit transport equation[13] and extracted $\mu_s'(\lambda)$ and $\mu_a(\lambda)$, the inverse of the reduced scattering and absorption mean-free paths, respectively. In the rest of this paper, $\mu_s'$ and $\mu_a$ will imply wavelength dependence. From $\mu_a$ they are able to extract hemoglobin oxygenation and concentration. From $\mu_s'$ and assuming Mie scattering, they obtain scatterer density and cross-section. A study of one normal and one adenomatous (polyp) tissue sample found the samples had different hemoglobin concentration and scattering cross-section. Amelink et. al. conducted DRS over different delivery-collection separations to measure blood oxygenation, blood concentration, average blood vessel diameter, and $\mu_s'$[14]. They used an optical fiber probe to deliver light to the tissue and collect reflectance. The delivery and collection fibers were spaced at several distances to collect light that traveled different distances in the tissue. Varying delivery-collection separation provides extra information for extracting tissue parameters. They measured 27 non-malignant spectra and 4 malignant spectra from

bronchial tissue of 9 patients. Biopsies were taken from the same locations and tissue state was assessed by a pathologist. The spectra were fitted to a reflectance model based on Monte Carlo simulations and blood vessel geometry[15]. They found malignant tissue has lower oxygenation, higher blood concentration, and smaller vessel diameter. Reflectance spectroscopy is very capable of measuring structural properties of tissue and is valuable for cancer diagnosis.

Raman, fluorescence, and reflectance spectroscopy, along with other forms of spectroscopic diagnosis, may soon be part of routine cancer screening procedures in multiple organs. The cellular level biochemical and structural information they provide are invaluable and nearly unattainable by conventional screening procedures. These techniques can be used in combination such that the combined diagnostic accuracy is greater than the accuracy of any individual technique. For example, our laboratory is working on a tri-modal spectroscopy (TMS) project that combines intrinsic fluorescence spectroscopy (IFS), DRS, and LSS[16]. IFS is fluorescence spectroscopy with the influences of scattering and absorption removed. DRS is used to isolate the fluorescence and single scattering signals from multiple scattering and absorption signals. Therefore, TMS can offer more accurate diagnosis than any of FS, LSS, or DRS alone. Spectroscopic diagnosis can also be extended to wide area surveillance from the small area studies presented in this section.

## 1.2 Spectroscopic Imaging

Spectroscopic modalities for cancer detection have been demonstrated effectively over small areas in multiple organs (Section 1.1). In the introduction we discussed frequenctly used imaging techniques and the information they provide. Extending spectroscopy to wide area imaging will enable spectroscopic diagnosis over multiple tissue sites. This greatly decreases the likelihood of missing a small cancerous growth and will reduce the time and cost of treatment. Spectroscopic imaging appears to be a simple extension of small area diagnosis, but a combination of physical constraints makes the jump non-trivial. In this section we present some research on spectroscopic imaging with fluorescence spectroscopy (FS) and reflectance spectroscopy (RES). We leave light scattering spectroscopy (LSS), the study of single backscattering spectra, imaging for chapter 3.

Benavides et. al. used a reconfigured colposcope to acquire 3.5cm diameter fluorescence images at multiple wavelengths from the cervix[17]. They used two excitation wavelengths, 345nm and 440nm, to uniformly illuminate a 3.5cm area of cervix and obtained the color images shown in figure 1.1. After processing with an algorithm developed during a small area FS study[18], they were able to map areas with high-grade dysplasia (potentially cancerous) versus squamous normal (cancer free) tissue. The mapping agreed with independent diagnosis determined by a pathologist.

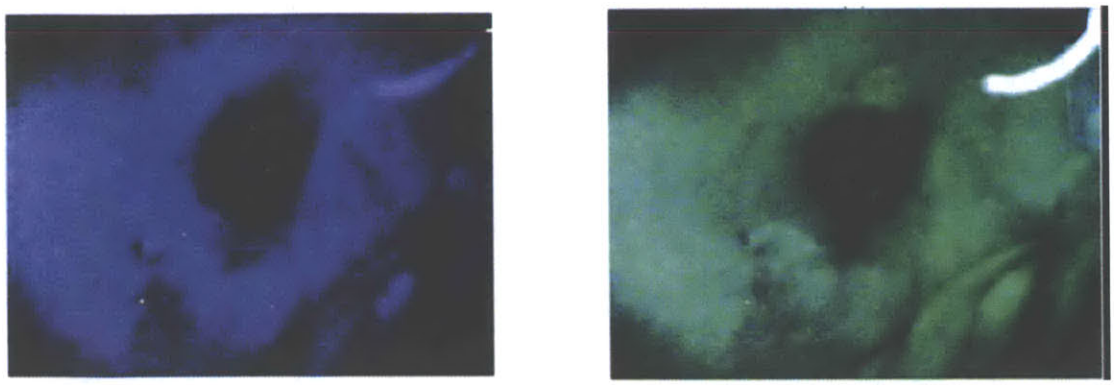

(a) 345nm image (b) 440nm image

Figure 1.1: Fluorescence images at two different excitation wavelengths acquired with a color CCD. Pictures courtesy of Benavides et. al.

Nordstrom et. al. conducted fluorescence and reflectance spectroscopy over a 3mm diameter area, divided into 120 regions, of cervix *in vivo*[19]. They studied 373 normal squamous tissue spectra, 25 CIN I (different degrees of cervical intraepithelial neoplasia) spectra, 52 CIN II/III spectra, and 40 metaplasia (transformation to abnormal tissue) spectra. A pathologist independently determined the classifications. With this set of data, the authors set up neural network training routines using part of the spectroscopic data and corresponding histology results. They applied the computed weights to the entire set and obtained the sensitivities and specificities in table 1.1. The authors found FS is able to diagnose disease better than RES but the latter is able to distinguish metaplasia from CIN, demonstrating that the modalities are complementary.

Table 1.1: Diagnostic performance of fluorescence and reflectance spectroscopy imaging system at all regions of all patients studied. Data courtesy of Nordstrom et. al.

| | Fluorescence | | Reflectance | |
|---|---|---|---|---|
| Tissue Classes | Sensitivity | Specificity | Sensitivity | Specificity |
| Normal vs. CIN II/III | 91% | 93% | 82% | 67% |
| Normal vs. CIN I | 86% | 87% | 70% | 65% |

| | | | | |
|---|---|---|---|---|
| Normal vs. Metaplasia | 90% | 87% | 64% | 66% |
| Metaplasia vs. CIN II/III | 18% | 84% | 77% | 76% |

The results of these studies demonstrate that for fluorescence and reflectance spectroscopy, wide area imaging has performance per region comparable to that of small area spectroscopic diagnosis. This is not surprising because an imaging system can be a small area system that is translated from measurement to measurement to acquire data over the entire area of interest (raster scanning). However, constraints such as data acquisition time may necessitate more advanced instrument designs. Fluorescence and reflectance spectroscopy imaging have been well demonstrated and are entering extensive clinical studies , but other spectroscopic modalities such as Raman spectroscopy and light scattering spectroscopy require greater incident light intensity and thus, have not progressed as far in imaging. There are many opportunities for research and development of spectroscopic imaging technology. In the remaining chapters we present progress on LSS imaging.

---

[1] C. Raman, K. Krishnan; "A New Type of Secondary Radiation"; Nature; Vol. 121 (1928).

[2] R. Cotran, V. Kumar, T. Collins; Pathologic Basis of Disease; W.B. Saunders Company (1999).

[3] U. Utzinger, D. Heintzelman, A. Mahadevan-Jansen, A. Malpica, M. Follen, R. Richards-Kortum; "Near-Infrared Raman Spectroscopy for *in Vivo* Detection of Cervical Precancers"; Applied Spectroscopy; Vol. 55, 955-9 (2001).

[4] C. Kendall, N. Stone, N. Shepherd, K. Geboes, B. Warren, R. Bennett, H. Barr; "Raman spectroscopy, a potential tool for the objective identification and classification of neoplasia in Barrett's oesophagus"; J. Pathol.; Vol. 200, 602-9 (2003).

[5] A. Haka, K. Shafer-Peltier, M. Fitzmaurice, J. Crowe, R. Dasari, M. Feld; "Diagnosing breast cancer by using Raman spectroscopy"; PNAS, Vol. 102, No. 35, 12371-12376 (2005).

[6] J. Lakowicz; Principles of Fluorescence Spectroscopy; Kluwer Academic/Plenum Publishers (1999).

[7] N. Ramanujam, M. Mitchell, A. Mahadevan, S. Thomsen, A. Malpica, T. Wright, N. Atkinson, R. Kortum; "Spectroscopic Diagnosis of Cervical Intraepithelial Neoplasia (CIN) *In Vivo* using Laser-Induced Fluorescence Spectra at Multiple Excitation Wavelengths"; Lasers in Surgery and Medicine; Vol. 19, 63-74 (1996).

[8] C. Wang, K. Chiang, C. Chen, C. Chiang, Y. Kuo, S. Chow; "Diagnosis of oral cancer by light-induced auto fluorescence spectroscopy using double excitation wavelengths"; Oral Oncology; Vol. 35, 144-150 (1999).

[9] M. Bard, A. Amelink, M. Skurichinac, M. den Bakkerd, S. Burgersa, J. van Meerbeecka, R. Duinc, J. Aertsa, H. Hoogstedena, H. Sterenborg; "Improving the specificity of fluorescence bronchoscopy for the analysis of neoplastic lesions of the bronchial tree by combination with optical spectroscopy: preliminary communication"; Lung Cancer; Vol. 47, 41-47 (2005).

[10] G. Zonios, L. Perelman, V. Backman, R. Manoharan, M. Fitzmaurice, J. Van Dam, M. Feld; "Diffuse reflectance spectroscopy of human adenomatous colon polyps *in vivo*"; Applied Optics, Vol. 38, No. 31, 6628-37 (1999).

[11] L. Perelman, V. Backman, G. Zonios, R. Manoharan, A. Nusrat, S. Shields, M. Seiler, C. Lima, T. Hamano, I. Itzkan, J. Van Dam, J. Crawford, M. Feld; "Observation of Periodic Fine Structure in Reflectance from Biological Tissue: A New Technique for Measuring Nuclear Size Distribution", Physical Review Letters; Vol. 80, No. 3, 627-30 (1998).

[12] R. Gurjar, V. Backman, L. Perelman, I. Georgakoudi, K. Badizadegan, I. Itzkan, R. Dasari, M. Feld; "Imaging human epithelial properties with polarized light-scattering spectroscopy"; Nature Medicine; Vol. 7, No. 11, 1245-48 (2001).

[13] T. Farrell, M. Patterson, B. Wilson, "A diffusion theory model of spatially resolved, stead-state diffuse reflectance for the non-invasive determination of tissue optical properties"; Med. Phys.; Vol. 19, 879-88 (1992).

[14] A. Amelink, H. Sterenborg, M. Bard, S. Burgers; "In vivo measurement of the local optical properties of tissue by use of differential path-length spectroscopy"; Optics Letters; Vol. 29, No. 10, 1087-9 (2004).

[15] R. van Veen, W. Verkruysse, H. Sterenborg; "Diffuse-reflectance spectroscopy from 500 to 1060nm by correction for inhomogeneously distributed absorbers"; Optics Letters, Vol. 27, No. 246, 246-8 (2002).

[16] I. Georgakoudi, B. Jacobson, J. Van Dam, V. Backman, M. Wallace, M. Muller, Q. Zhang, K. Badizadegan, D. Sun, G. Thomas, L. Perelman, M. Feld; "Fluorescence, reflectance, and light-scattering spectroscopy for evaluating dysplasia in patients with Barrett's esophagus"; Gastroenterology, Vol. 120, 1620-9 (2001).

[17] J. Benavides, S. Chang, S. Park, R. Richards-Kortum, N. Mackinnon, C. MacAulay, A. Milbourne, A. Malpica, M. Follen; "Multispectral digital colposcopy for *in vivo* detection of cervical cancer"; Optics Express; Vol. 11, No. 10, 1223-36 (2003).

[18] S. Chang, M. Follen, A. Malpica, U. Utzinger, S. Gtaerkel, D. Cox, N. Atkinson, C. MacAulay, R. Richards-Kortum; "Optimal excitation wavelengths for discrimination of cervical neoplasia"; IEEE Trans. Biomed. Eng.; Vol. 49, 1102-11 (2002).

[19] R. Nordstrom, L. Burke, J. Niloff, J. Myrtle; "Identification of Cervical Intraepithelial Neoplasia (CIN) Using UV-Excited Fluorescence and Diffuse-Reflectance Tissue Spectroscopy"; Lasers in Surgery and Medicine; Vol. 29, 118-127 (2001).

# Chapter 2

# Principles of light scattering in tissue

In Chapter 1 we briefly reviewed research on frequently used spectroscopic diagnosis modalities: Raman spectroscopy, fluorescence spectroscopy, and reflectance spectroscopy. We also reviewed some research on spectroscopic imaging. In section 2.1 of this chapter, we present a two-layer model of elastic light scattering in tissue. Light scattered by tissue under this model is made up of two contributions, single backscattering (SBS) and multiple scattering/diffusive background. In this chapter, we focus on the principal spectroscopic modality of this thesis, light scattering spectroscopy (LSS), the study of single elastic backscattering spectra. Separating SBS from background is the topic of chapter 3. Sections 2.2 through 2.5 provide a quantitative description of light scattering and present powerful findings. The primary objectives of these sections are to introduce and justify our use of the Mie theory and single particle scattering approximations to analyze LSS results in chapter 4. Most of the material discussed in these sections comes from two frequently used textbooks on light scattering[1] [2]. With a greater understanding of scattering, we can analyze LSS signals in detail to obtain information about scatterers in tissue.

## 2.1 Two-layer tissue model

To understand light scattering spectroscopy in tissue, we present a two-layer tissue model in figure 2.1. The top layer consists of epithelial cells and their organelles. The epithelial nuclei here are the primary scatterers because they have a large index of refraction mismatch with the surrounding medium[3]. Smaller organelles in the epithelium

such as mitochondria, which are more numerous, also scatter[4]. The lower layer consists of underlying tissue.

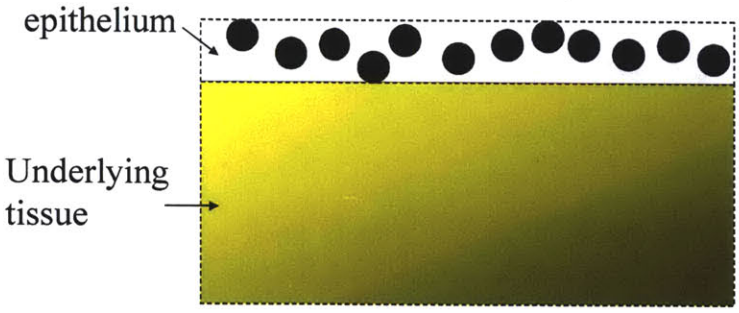


Figure 2.1: Two-layer tissue model for light scattering spectroscopy.

Approximately 5% of the illumination light exciting the tissue is singly backscattered by organelles in the epithelium. Most of the light penetrates the epithelium and is absorbed or undergoes further scattering events. Light returning from the underlying tissue contributes multiple scattering and diffuse reflectance. Since most epithelial cancers originate in the superficial cells of the epithelium[5], the origin of single backscattering, LSS is an ideal technique for detecting the earliest stages of cancer. LSS can also be implemented in an imaging modality for wide area diagnosis.

## 2.2 Principles of light scattering from a single particle

The theory of light scattering from a single particle is the foundation of our research. When an electromagnetic wave is incident on a particle with refractive index different from its surrounding medium, secondary radiation is released in all directions. The secondary radiation is the scattering. Many physical phenomena are due to light scattering. The color of the sky and diffuse reflection off an optically rough surface (roughness > light wavelength $\lambda$ / 4) are two examples. For a small particle (size

comparable to $\lambda$) with homogeneous index of refraction, the angular variation of the scattered light depends on $\lambda$, indices of refraction of the particle and the medium, particle size, and particle shape. Regardless of the complexity of the particle and medium, the scattering is determined by Maxwell's equations.

We can separate the study of light scattering into two problems, the direct and the inverse scattering problems. The direct problem asks for the scattered electric field given the incident field and the properties of the particle (scatterer). This can be found by solving Maxwell's equations, but the process may be difficult for complex configurations. The inverse problem asks for the scatterer's properties given the incident and scattered fields. This is usually the problem of interest in light scattering experiments, including our cancer diagnosis objectives. Unfortunately, to precisely determine the particle's properties, we should know the amplitude and phase of the scattered field at all points in space, which is not usually attainable in practice. In biomedical applications, typically only the amplitude of the scattered field on a plane (camera) is known. To aid the identification process, we can usually make some assumptions about the particle's properties, such as physically feasible ranges for shape, size, and index of refraction. Nevertheless, a unique solution is not guaranteed from a given measurement.

To prepare for the inverse problem, we begin by reviewing the direct problem. Light propagation in matter is described by Maxwell's equations (SI units).

$$
\begin{aligned}
\nabla \bullet \mathbf{D} &= \rho_F \\
\nabla \times \mathbf{E} + \frac{\partial \mathbf{B}}{\partial t} &= 0 \\
\nabla \bullet \mathbf{B} &= 0 \\
\nabla \times \mathbf{H} &= \mathbf{J}_F + \frac{\partial \mathbf{D}}{\partial t} \\
\mathbf{D} &= \varepsilon_0 \mathbf{E} + \mathbf{P} \\
\mathbf{H} &= \frac{\mathbf{B}}{\mu_0} - \mathbf{M}
\end{aligned}
\tag{2.1}
$$

**E** is the electric field, **B** the magnetic induction, **D** the electric displacement, **H** the magnetic field, **P** the electric polarization, **M** the magnetization, $\varepsilon_o$ the permittivity, $\mu_o$ the permeability of free space, $\rho_F$ the charge density, and $\mathbf{J_F}$ the current density. To close the system of equations, Maxwell's equations require information about the medium of propagation, which are provided by the constitutive relations.

$$
\begin{aligned}
\mathbf{J}_F &= \sigma \mathbf{E} \\
\mathbf{B} &= \mu \mathbf{H} \\
\mathbf{P} &= \varepsilon_0 \chi \mathbf{E}
\end{aligned}
\tag{2.2}
$$

$\sigma$ is the conductivity, $\mu$ is the permeability, and $\chi$ is the electric susceptibility of the medium. For linear, homogeneous, and isotropic media, $\sigma$, $\mu$, and $\chi$ are constant scalars. Solving Maxwell's equations with the constitutive relations and boundary conditions to describe the particle's borders completely solves the direct problem.

Maxwell's equations in full-form are not easy to solve. Finite difference time domain (FDTD) algorithms solve Maxwell's equations at every spatial position and every step in time[6], but these are computation intensive and usually make some assumptions about the electric and magnetic fields. Often times, the electric and magnetic fields have

time and spatial dependences. A monochromatic (one wavelength) light wave has irradiance, frequency ($1/\lambda$), and polarization. Irradiance is the power per unit area incident on a surface in a direction normal to the surface. Polarization is the orientation of **E** and how that changes over time. Linearly polarized light has **E** oscillating along a constant direction. Elliptically polarized light has **E** changing its magnitude and direction in such a way that the electric field vector traces an ellipse. The polarization state of an electromagnetic wave can be described by its Stokes vector with parameters $I$, $Q$, $U$, and $V$.

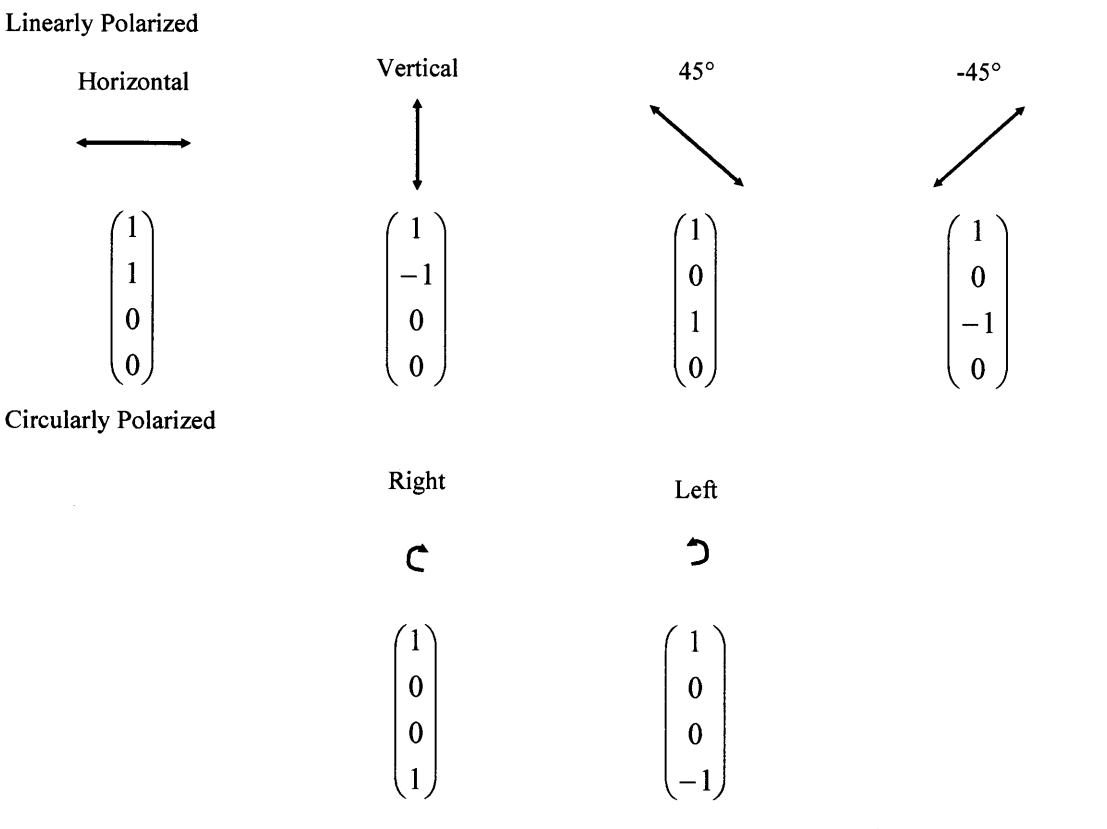


Courtesy of Bohren and Huffman

Refer to the text by Bohren and Huffman for the definition of the Stokes parameters. Of note, for unpolarized light, the stokes vector has $I = 1$ and all other parameters zero. The

usefulness of the Stokes vector is that its transformation after passage through an optical element can be described by a linear matrix multiplication. This matrix is called the Mueller matrix and it can be used to describe a scattering event.

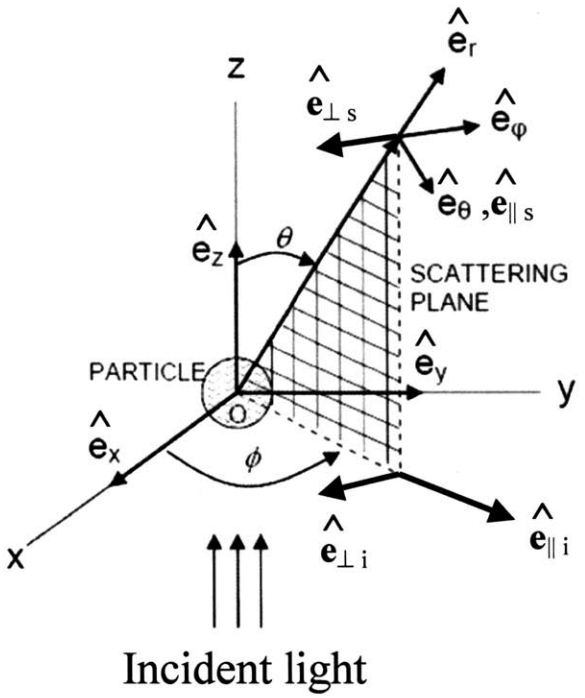


Figure 2.2: Geometry of light scattering. Adapted from Scepanovic et. al.[7] and Bohren and Huffman.

The geometry of light scattering is illustrated in figure 2.2. The incident electric field $\mathbf{E_i}$ is along $\mathbf{e_z}$ and the scattered field $\mathbf{E_s}$ is along $\mathbf{e_r}$. $\mathbf{E_i}$ is polarized along $\mathbf{e_x}$. $\theta$, the scattering angle, is the angle between $\mathbf{e_z}$ and $\mathbf{e_r}$. The plane containing $\mathbf{e_z}$ and $\mathbf{e_r}$ is the scattering plane and the angle between it and $e_x$ is $\phi$, the azimuthal angle. Note that $\phi$ is not defined for unpolarized illumination. That means there is no $\phi$-asymmetry (azimuthal asymmetry) with unpolarized illumination or at $\theta = 180°$. The $i$ and $s$ subscripts indicate incident and scattered fields while $\|$ and $\perp$ indicate field components parallel and

perpendicular to the scattering plane. With this notation, the relation between incident and scattered electric fields can be written in the form:

$$\begin{pmatrix} E_{\parallel s} \\ E_{\perp s} \end{pmatrix} = \frac{e^{ik(r-z)}}{-ikr} \begin{pmatrix} S_2 & S_3 \\ S_4 & S_1 \end{pmatrix} \begin{pmatrix} E_{\parallel i} \\ E_{\perp i} \end{pmatrix} \tag{2.3}$$

$k$ is the wave number in the medium and $r$ is the distance to the detector. $S_1$, $S_2$, $S_3$, and $S_4$ form the amplitude scattering matrix and depend on particle size, shape, index of refraction, $\theta$, and $\phi$. The scattering Mueller matrix also depends on the $S$ terms. In medical imaging, the scattering Mueller matrix is usually of interest because it directly provides the irradiance and polarization of the scattered light.

Equation 2.3 is the solution to the direct elastic light scattering problem, although the $S$ terms may not be easy to compute. Before presenting approximate and rigorous solutions to equation 2.3, we review some commonly used scattering terminology. Let $W_{sca}$ be the total power scattered by a particle illuminated with irradiance $I$. The scattering cross-section is defined as $C_{sca} = W_{sca} / I$. If we consider the cross-section in some small solid angle $d\Omega$, we obtain the differential scattering cross section $dC_{sca} / d\Omega$, which is a function of $\theta$ and $\phi$. From $C_{sca}$, we can also define the scattering efficiency $Q_{sca} = C_{sca} / G$, where $G$ is the geometric cross-section of the particle, the amount of area occupied by the particle in the path of the incident wave. $dC_{sca} / d\Omega$ is very useful for the $\phi$/LSS technique we present in chapter 3 and $Q_{sca}$ has been the basis of much LSS research.

## 2.3 Scattering by particles smaller than the wavelength

For scatterers that satisfy certain criteria, the $S$ terms take the form of simple expressions that provide insight to scattering dynamics and suggest possible advancements. Scattering from particles with size << $\lambda$ can be described by Rayleigh scattering, where the $S$ terms take the simple form:

$$\begin{pmatrix} S_2 & S_3 \\ S_4 & S_1 \end{pmatrix} = ik^3\alpha \begin{pmatrix} \cos\theta & 0 \\ 0 & 1 \end{pmatrix} \tag{2.4}$$

$\alpha$ is the polarizability of the particle. For particles with refractive index close to that of the surrounding medium, $m = n_{particle} / n_{medium} \approx 1$, the polarizability is:

$$\alpha = \frac{(m-1)V}{2\pi}$$

$V$ is the volume of the particle. In tissue, most cell organelles have $m$ close to unity[8]. Note from equation 2.4 the $S_3$ and $S_4$ terms vanish, leading to a simplification of the scattering Mueller matrix. From equation 2.3, we find the scattered irradiance has $\lambda^{-4}$ dependence. We also observe from equation 2.3 the magnitude of $I_{\phi=0} = |E_{\| i}|^2$ varies as $\cos^2\theta$ and $I_{\phi=90} = |E_{\perp i}|^2$ is constant in angle. Thus, near the direct backscattering direction, $\theta = 180°$, of interest to *in vivo* imaging, $I_{\phi=0} \approx I_{\phi=90}$. The $\phi$/LSS technique we present in chapter 3 exploits the fact that larger particles exhibit greater azimuthally asymmetric scattering around direct backscattering.

In tissue, Rayleigh scattering is only valid for the smallest of cell organelles. Larger organelles such as the nucleus and mitochondria have sizes close to or larger then the wavelength. A less restrictive theory is Rayleigh-Gans scattering, which is accurate for particles that satisfy:

$$|m-1| << 1$$
$$2ka|m-1| << 1 \tag{2.5}$$

$a$ is a length characterizing the size of the particle. For spheres, $a$ is the radius. $S_3$ and $S_4$ are still zero, but $S_1$ and $S_2$ now take the form:

$$S_1 = -\frac{ik^3}{2\pi}(m-1)Vf(\theta,\phi)$$
$$S_2 = -\frac{ik^3}{2\pi}(m-1)Vf(\theta,\phi)\cos\theta \tag{2.6}$$

The form factor $f$ depends on particle shape and varies with angle. For a homogeneous sphere, $f = 3(\sin u - u \cos u) / u^3$, where $u = 2x \sin(\theta/2)$ and $x = k\,a$. From equation 2.3 and the form factor for spheres, we again see that the scattered irradiance has $\lambda^{-4}$ dependence and $I_{\phi=0} \approx I_{\phi=90}$ around $\theta = 180°$. Therefore, Rayleigh-Gans scattering also exhibits minimal azimuthal asymmetry.

The Rayleigh and Rayleigh-Gans approximations are relatively simple descriptions of light scattering that are relevant for scatterers smaller than the wavelength or with small index mismatch $m$ from the medium. These well describe scattering from smaller subcellular organelles in tissue. Numerous researchers use these models to describe scattering from biological samples[9] [10]. Simple solutions to the direct problem lead to easy solutions to the inverse problem.

## 2.4 Scattering by a homogeneous sphere of arbitrary size

The Rayleigh and Rayleigh-Gans approximations provide relatively simple solutions to the inverse problem, but they do not describe a lot of interesting scattering effects from large particles. Since our primary interest is light scattering from cell nuclei (diameter = 4 – 20$\mu$m[11]) that are significantly larger then visible light wavelengths ($\lambda$ = 400 – 700nm), we look for a formulation that relaxes the constraints on particle size and index. The next step up in complexity is the solution to the direct problem of scattering from a homogeneous sphere of arbitrary size and index of refraction. In this section we will not present the equations for the $S$ terms, since their complexity limits physical insight. Instead, we present numerical computations of scattering from spheres and discuss qualitative results relevant to our work. The matlab program for this was developed based on a code provided in Bohren and Huffman.

Scattering by a homogeneous sphere illuminated with a plane wave is described by Mie theory, named after Gustav Mie, who formulated the solution in 1908*. Mie theory is an exact solution of Maxwell's equations with boundary conditions defined by the sphere's surface. The solution has $S_3$ and $S_4$ equal to zero, but $S_1$ and $S_2$ are infinite sums of Bessel functions. The important input parameters are the incident Stokes vector, diameter of the sphere $d$, $m$, $\lambda$ in the medium, $\theta$, and $\phi$. Figure 2.3 shows the elastic scattering irradiance spectrum at $\theta = 180°$ from a sphere of diameter $d = 0.01\mu$m and $m$ = 1.05 over the visible wavelengths.

* It is debated whether Gustav Mie first solved the spheres scattering problem, but for historical consistency, we refer to the solution as Mie theory.

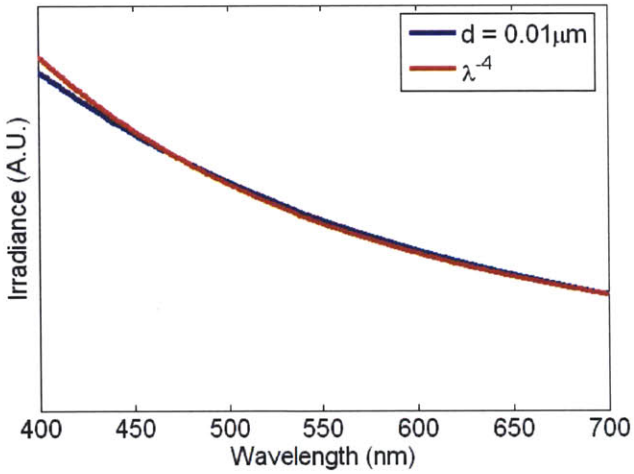


Figure 2.3: Scattering from a $d = 0.01\mu$m sphere and the $\lambda^{-4}$ dependence of scattering from small spheres predicted by the Rayleigh and Rayleigh-Gans approximations. Both spectra have been divided by their respective means for comparison.

As expected, Mie theory reduces to the Rayleigh approximation of equation 2.4 when $d << \lambda$. For larger sizes, we see departure from the $\lambda^{-4}$ dependence of the small particle approximations. Figure 2.4 shows the scattering spectrum with $d = 10\mu$m.

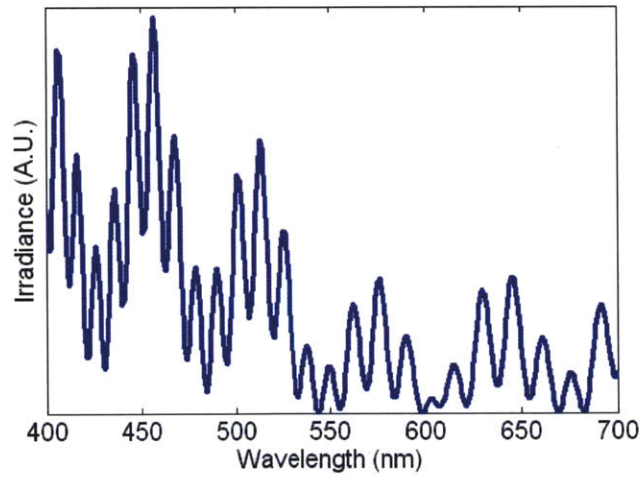


Figure 2.4: Scattering from $d = 10\mu$m sphere, $m = 1.05$, $\theta = 180°$.

There are multiple orders of oscillation frequencies in the spectrum coming from the sum of Bessel functions. A fourier transform will reveal multiple peaks. Perelman et. al. observed that larger spheres scatter with higher oscillation frequency and used that phenomenon to identify scatterer size. Large particle scattering also exhibits azimuthal asymmetry. Figure 2.5 plots $I_{\phi=0}(\theta)$ and $I_{\phi=90}(\theta)$ as functions of $\theta$ at $\phi = 0°$ and $\phi = 90°$ and a fixed wavelength $\lambda = 500$nm. The incident illumination is linearly polarized.

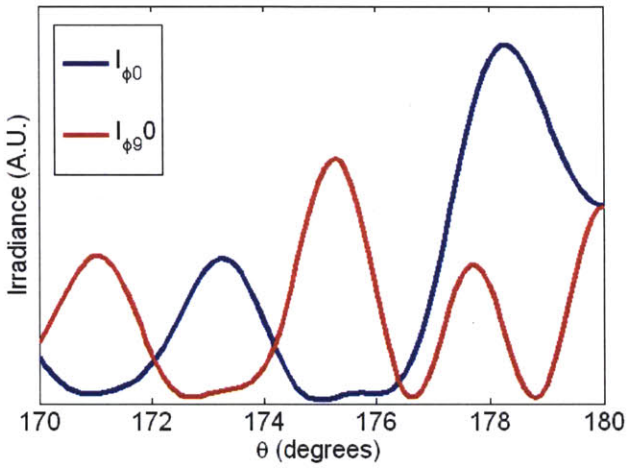


Figure 2.5: Scattering from $d = 10\mu$m sphere and $m = 1.05$ at $\lambda = 500$nm, $\theta =$ from 170° to 180°, and $\phi = 0°$ and 90°.

Unlike the Rayleigh and Rayleigh-Gans approximations, Mie theory shows that large spheres exhibit azimuthal asymmetry near direct backscattering. A spectral plot about $\theta =$ 178°, figure 2.6, shows azimuthal asymmetry varies with wavelength.

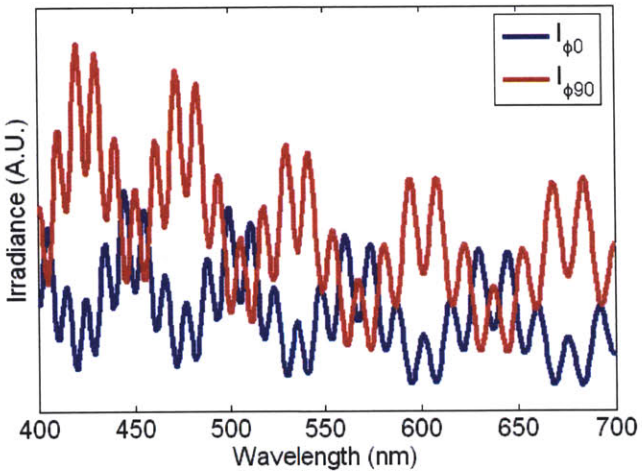


Figure 2.6: $I_{\phi=0}$ and $I_{\phi=90}$ at $\theta = 178°$ and m = 1.05 for d = 10$\mu$m sphere. The incident wave is linearly polarized.

Mie theory exactly describes scattering by a homogeneous sphere and can be used to solve the inverse problem, which we will demonstrate in chapter 4. It is our model of choice for inverting LSS spectra measured from tissue to extract the scatterer's parameters. However, scatterers in tissue can be aspherical and inhomogeneous. Accounting for these adds an element of asymmetry to the equations and leads to much more complex solutions. Also, sections 2.2 – 2.4 have only considered single particle scattering. Scattering from a collection of particles can potentially be much more complicated. In the next section, we argue for using Mie theory to describe scattering from tissue.

### 2.5 Scattering by a tissue-like collection of non-ideal particles

Sections 2.2 – 2.4 considered single particle scattering and arrived at Mie theory, which describes scattering by a homogeneous sphere illuminated by a plane wave. In human epithelial tissue and most biological systems, more then one particle is excited by

the illumination, and these particles are aspherical, inhomogeneous, and oriented in various configurations. Also, index of refraction changes may be continuous[12], but we will limit our analysis to discrete variations such as individual particles. A number of research groups have used Mie theory to model light scattering from biological samples[13] [14]. This section provides physical justification for the use of Mie theory to describe elastic light scattering from tissue and discusses some avenues for future research.

In a medium with only one particle, the illumination wave excites the particle and scattering occurs. When multiple particles are present, the illumination excites all the particles and all of them scatter. The scattered radiation can then excite further scattering by neighboring particles (multiple scattering). Also, scattered waves may interfere with each other before reaching the detector. Scattering by a collection of particles, even identical particles, can be quite complicated. Ideally, we want to be able to approximate the total scattering intensity from all particles by the sum of the scattering intensities from individual particles. We call this approximation single particle scattering. For this to be accurate, two conditions must be met: (1) particles must be sufficiently spaced such that scattered fields do not interfere with each other prior to reaching the detector; and (2) the total scattered field in any region of the sample is weak compared to the illumination field (weak scattering). In biological tissue, cell membranes are in contact with other cell membranes and all cells have numerous organelles, all of which scatter because they have different index of refractions than the surrounding media. However, criterion (1) can still be satisfied if interference between scattering fields from the tissue is averaged such that total field intensity is the sum of individual field intensities. Using incoherent excitation

light can accomplish this. Criterion (2) is satisfied when we selectively observe the SBS signals from epithelial nuclei, which are close to the surface. These scatterers have higher refractive index than other organelles and are important for cancer diagnosis [15]. To selectively observe SBS from epithelial nuclei, we must remove the effects of multiple scattering and diffuse reflectance from other epithelial organelles and lower tissue layers. To visualize this, consider the enlargement of the top layer of figure 2.1 (figure 2.7).

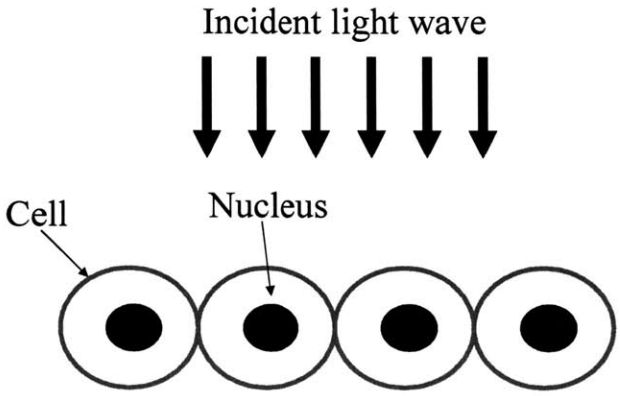


Figure 2.7: Single elastic backscattering model of epithelial tissue.

Single backscattering, the key information for LSS, can only occur at the most superficial cell layers (epithelium). To comply with criterion (2), assuming the influences of scattered fields from non-nuclei organelles and lower tissue layers are removed, the singly scattered fields from epithelial nuclei must be much weaker than the illumination field throughout the epithelium. Large scatterers such as nuclei scatter predominantly in the forward direction, $\theta = 0°$. Since forward scattering goes directly into the lower tissue layers, by our model of light scattering in tissue (figure 2.1), criterion (2) is satisfied. It is important to remove the effects of multiple scattering and diffuse reflectance because these scattered fields are comparable in intensity to the incident field. Chapter 3 discusses techniques to isolate SBS from tissue, which enable LSS.

We have justified using single particle scattering to describe SBS by a collection of epithelial nuclei. However, this does not necessarily support the use of Mie theory analysis, which assumes spherical and homogeneous scatters, because nuclei are in general aspherical and inhomogeneous. Here, we provide several justifications for approximating with a sphere. The primary goal of this research is to detect cancer, and two features of cancer are nuclear enlargement and hyperchromasia (higher index of refraction)[5]. Therefore, the scattering theory must account for size and index differences to enable solving the inverse problem. Mie theory has size and index dependence, but more advanced theories such as ellipsoid scattering may lead to more accurate inversion for the particle's shape. However, a theory of scattering by ellipsoids is much more complicated because an ellipsoid has 3 axes and 3 orientation angles, compared to just one diameter parameter for a sphere. In tissue, we measure SBS from a randomly oriented collection of aspherical particles. The effects of particle orientation are then averaged. Bohren and Huffman show that for a collection of randomly oriented cylinders, the total scattered field is similar to that from a collection of spheres. Another approximation made by Mie theory is homogeneity of index of refraction. In nuclei, DNA clumping can lead to heterogeneity. Chen et. al. used FDTD simulations to compute scattering from randomly inhomogeneous spheres[16]. They found that the spectral dependence of the total scattering cross section ($C_{sca}$) is very similar to that of a sphere with refractive index averaged over the volume. These results validate the use of Mie theory and the single particle approximation to solve the inverse SBS problem crucial to light scattering spectroscopy.

The arguments and experiments above show that the Mie theory and single particle scattering approximations are adequate for describing LSS spectra. However, the limits of using Mie theory to model light scattering from biological systems can be further investigated. Future research can look into the maximum deviation from spherical shape tolerated by Mie theory for a collection of particles. Also, the effects of inhomogeneity at specific angles can be studied. These topics are not the focus of this thesis, but part of our future research will be to study the accuracy of Mie theory in biological systems. The remainder of this thesis will present previously developed and novel techniques for removing the multiple scattering and diffuse background signals returning from tissue to isolate the SBS signal required for LSS. This will allow the Mie theory and single particle scattering approximations to be applied.

---

[1] C. Bohren, D. Huffman; Absorption and Scattering of Light by Small Particles; Wiley-VCH Verlag GmbH & Co. KgaA (2004).

[2] H. van de Hulst; Light Scattering by Small Particles; Dover Publications, Inc. (1981).

[3] L. Perelman, V. Backman, G. Zonios, R. Manoharan, A. Nusrat, S. Shields, M. Seiler, C. Lima, T. Hamano, I. Itzkan, J. Van Dam, J. Crawford, M. Feld; "Observation of Periodic Fine Structure in Reflectance from Biological Tissue: A New Technique for Measuring Nuclear Size Distribution", Physical Review Letters; Vol. 80, No. 3, 627-30 (1998).

[4] J. Mourant, M. Canpolat, C. Brocker, O. Esponda-Ramos, T. Johnson, A. Matanock, K. Stetter, J. Freyer; "Light scattering from cells: the contribution of the nucleus and the effects of proliferative status"; Journal of Biomedical Optics; Vol. 5, No. 2, 131-7 (2000).

[5] R. Cotran, V. Kumar, T. Collins; Pathologic Basis of Disease; W.B. Saunders Company (1999).

[6] D. Arifler, M. Guillaud, A. Carraro, A. Malpica, M. Follen, R. Richards-Kortum; "Light Scattering from Normal and Dysplastic Cervical Cells at Different Epithelial Depths: Finite Difference Time Domain Modeling with a Perfectly Matched Layer Boundary Condition"; Journal of Biomedical Optics; Vol. 8, 484-94 (2003).

[7] O. Scepanovic; Light scattering spectroscopy clinical imaging device implementation; Masters thesis; MIT Department of Electrical and Computer Science (2003)

[8] A. Dunn; Light Scattering Properties of Cells; PhD thesis; Graduate School of The University of Texas Austin (1997).

[9] D. Cross, P. Latimer; "Angular Dependence of Scattering from Escherichia Coli Cells"; Applied Optics; Vol. 11, No. 5, 1225-8 (1972).

[10] P. Sloot, A. Hoekstra, C. Figdor; "Osmotic Response of Lymphocytes Measured by Means of Forward Light Scattering: Theoretical Considerations"; Cytometry; Vol. 9, 636-41 (1988).

[11] V. Backman, R. Gurjar, K. Badizadegan, I. Itzkan, R. Dasari, L. Perelman, M. Feld; "Polarized Light Scattering Spectroscopy for Quantitative Measurement of Epithelial Cellular Structures In Situ"; IEEE Journal of Selected Topics in Quantum Electronics; Vol. 5, No. 4, 1019-26 (1999).

[12] J. Schmitt, G. Kumar; "Turbulent Nature of Refractive Index Variations in Biological Tissue"; Optics Letters; Vol. 21, No. 16, 1310-2 (1996).

[13] J. Mourant, T. Johnson, V. Doddi, J. Freyer; "Angular dependent light scattering from multicellular spheroids"; Journal of Biomedical Optics; Vol. 7, No. 1, 93-99 (2002).

[14] M. Bartlett, G. Huang, L. Larcom, H. Jiang; "Measurement of particle size distribution in mammalian cells *in vitro* by use of polarized light spectroscopy"; Applied Optics; Vol. 43, No. 6, 1296-1307 (2004).

[15] V. Backman, V. Gopal, M. Kalashnikov, K. Badizadegan, R. Gurjar, A. Wax, I. Georgakoudi, M. Mueller, C. Boone, R. Dasari, M. Feld; "Measuring Cellular Structure at Submicrometer Scale With Light Scattering Spectroscopy"; IEEE Journal on Selected Topics in Quantum Electronics; Vol. 7, No. 6, 887-93 (2001).

[16] Z Chen, A. Taflove, V. Backman; "Equivalent volume-averaged light scattering behavior of randomly inhomogeneous dielectric spheres in the resonant range"; Optics Letters; Vol. 28, No. 10, 765-7 (2003).

# Chapter 3

# Techniques for isolating single backscattering

In chapter 2 we showed that identifying the single backscattering (SBS) contribution to a reflectance spectrum dominated by multiple scattering and diffuse reflectance is crucial for light scattering spectroscopy (LSS). Section 3.1 reviews previous research addressing this challenge. We have developed two novel differential measurements, space differential LSS (SD/LSS) and $\phi$-angle differential LSS ($\phi$/LSS), which isolate the SBS signal and potentially offer additional advantages. Sections 3.2 and 3.3 present the theory of SD/LSS and $\phi$/LSS respectively. Section 3.4 discusses the use of SD/LSS and $\phi$/LSS together in a wide-area imaging modality.

## 3.1 LSS research

Light scattering spectroscopy (LSS) is the study of single elastic scattering spectra. SBS is a small portion of the total reflectance (< 5%[1]) from tissue illuminated with light. Most of the reflectance is diffuse reflectance, which can be used for diffuse reflectance spectroscopy (section 1.1). In chapter 2 we discussed the importance of isolating the single backscattering signal from epithelial nuclei to using LSS for cancer detection. In this section we focus on LSS research that has led to techniques for isolating nuclear SBS. Many researchers have also used LSS to study smaller organelles such as mitochondria[2 3], but we will not review these works here.

Perelman et. al. measured reflectance from tissue over the wavelength range 350 - 650nm. They then modeled the reflectance as consisting of three components. The first

component is diffuse reflectance from lower tissue layers, as in the tissue model of figure 2.1. The second component is SBS and the third component is forward scattering from the epithelium caused by light returning from underneath. The authors assumed nuclei were the dominant scatterers in the epithelial layer because of their higher index of refraction. They found forward scattering and backscattering components oscillate out of phase with each other[4]. Thus, the epithelial nuclear scattering has oscillatory features. This can be seen in the van de Hulst approximation for the scattering cross section of a sphere[5], where the frequency of oscillation increases with scatterer size. As a result, a fourier transform of the reflectance spectrum will identify the size of nuclei in the tissue. To observe the oscillatory component introduced by epithelial nuclei, the authors used the diffuse reflectance model of Zonios et. al to remove multiple scattering and diffuse reflectance contributions from underlying tissue[6]. The scattering and absorption parameters were varied until the diffuse reflectance best fit the reflectance, then a difference yielded the oscillatory structure introduced by nuclei.

Accuracy of the above method relied on diffuse reflectance being well described by the model, which may vary between tissue types. Also, fourier transform over a finite wavelength range may lead to inaccurate results (leakage). Backman et. al. provided a more robust method by using polarization to separate nuclear SBS from diffuse reflectance[7]. They illuminated the tissue surface with linearly polarized and collimated light and measured reflectance in the exact backwards direction ($\theta = 180°$). With this configuration, SBS will predominantly be polarized in the same direction ($I_{ss} = I_{ss,\,||}$) while diffuse reflectance will have roughly equal amounts of both ($I_d = I_{d,\,||} + I_{d,\,\perp}$ with $I_{d,}$

$_{||} \approx I_{d,\perp}$). The total reflectance is $I_{ss} + I_d$. The authors used a polarizer (analyzer) to select the polarization of light collected. They took the difference between measurements parallel $I_{||} = I_{ss,||} + I_{d,||}$ and perpendicular $I_{\perp} = I_{d,\perp}$ to the incident polarization to yield $I_{||}$ - $I_{\perp} = I_{ss,||}$. This technique, called polarization LSS (P/LSS), isolates the SBS spectrum from epithelial nuclei. Backman et. al. used Mie theory to invert the spectra and extract size information from the scatterers. Gurjar et. al. applied P/LSS to wide area imaging of colon ademonas over a 1.69cm$^2$ area with distinct 125 x 125$\mu$m regions of diagnosis[8]. They mapped areas at risk of dysplasia by measuring the size of scatterers to identify regions with unusually large nuclei. Figure 3.1 maps regions with larger nuclei by imposing false color. Such a mapping is a typical LSS imaging diagnosis.

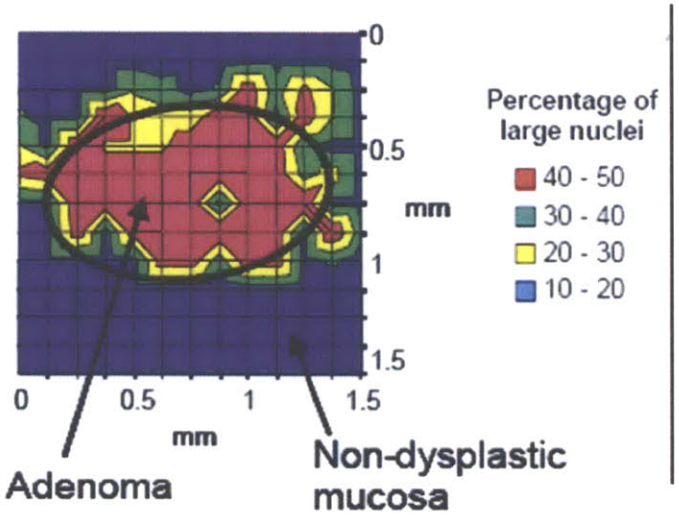


Figure 3.1: False color map of nuclear enlargement. Courtesy of Gurjar et. al.

P/LSS is more robust than the diffuse reflectance model approach because no assumptions are made about scattering and absorption beneath the epithelium. However, P/LSS assumes the polarization of multiply scattered light, which includes diffuse reflectance, is randomized. In the rest of this thesis, we loosely refer to randomization of

polarization as depolarized. By definition, diffuse reflectance is depolarized, but light that has only undergone a few scattering events may not be completely depolarized. Therefore, $I_{||}$ - $I_{\perp}$ may leave some multiple scattering residue. Also, P/LSS requires multiple polarization optics, which may greatly reduce the optical efficiency of the system. If we can isolate SBS while minimizing the use of polarizers, the system will provide a diagnosis in less time. In the next two sections we present SD/LSS and $\phi$/LSS improve the robustness and accuracy of LSS for cancer detection.

### 3.2 Space differential LSS

SD/LSS exploits the fact that SBS returns from the exact position the incident light illuminated the scatterer while multiple scattering and diffuse reflectance may return at distant regions of the tissue surface. Therefore, if we illuminate the tissue with a dark spot pattern (figure 3.2a), the illuminated areas ($I_L = I_{ss} + I_{ms}$) will contain SBS and multiple scattering while the non-illuminated areas ($I_D = I_{ms}$) will only have multiple scattering (figure 3.2b). Multiple scattering includes diffuse and non-diffuse light that have undergone multiple scattering events. The difference $I_{SD} = I_L - I_D$ yields SBS. To conduct light scattering spectroscopy, the pattern of figure 3.2a is imaged onto the tissue with different illumination light wavelengths and $I_{SD}(\lambda) = I_L(\lambda) - I_D(\lambda)$ is acquired at each wavelength.

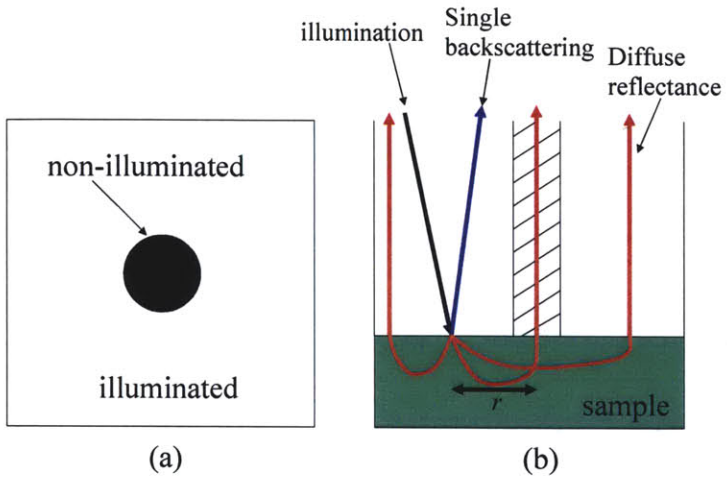


Figure 3.2: (a) Dark spot illumination pattern. (b) Propagation of singly backscattered and diffusely reflected light in tissue.

Like P/LSS, SD/LSS is not perfect at isolating single backscattering because multiple scattering can return within a very short distance of the illumination point. For any light path within the tissue with return distance $r$ (figure 3.2b) smaller than the radius of the dark spot, the intensity of multiply scattered light following the light path will not be fully accounted for in light collected from the dark spot. This means $I_{SD} = I_L - I_D$ will not completely isolate the SBS contribution. In chapter 4 we will use a light diffusion model tailored for light scattering in tissue to estimate the effectiveness of SD/LSS for a given dark spot size. The performance of SD/LSS is limited by spatial resolution of an imaging system, which is determined by numerical aperture (NA) of the collection optics[9] and CCD pixel size. If the numerical aperture is the limiting factor*, Rayleigh's criterion yields a minimum spatial resolution of $\Delta l = 0.61\ \lambda$ / NA. Therefore, the radius of the dark spot cannot be less than the minimum spatial resolution.

* So far we have found this to be the case because our unit areas occupy at least hundreds of pixels on the CCD.

Other research groups have used patterned illumination to extract extra information from samples. Cuccia et. al.[10] and Neil et. al.[11] use a spatially modulated sinusoidal illumination to gain scattering and absorption information at different depths. They found that using an illumination with higher spatial frequency is sensitive to more superficial features while lower frequencies penetrate deeper.

### 3.3 $\phi$-angle differential LSS

Polarization LSS and space differential LSS utilized the depolarization and penetration abilities of diffuse reflectance. They extracted the SBS signal from reflectance spectra dominated by multiple scattering signals. In this section, we present $\phi$/LSS, which utilizes the isotropic nature of diffuse reflectance and small particle SBS to specifically extract SBS from large scatterers.

For singly backscattered light ($\theta$~180°) with the same polarization as the incident light, we plot the angular scattering intensity maps of scatterers with diameter $d$ = 10$\mu$m, 5$\mu$m, and 2$\mu$m, calculated with Mie theory (figure 3.3). These polar plots plot scattering intensity at one wavelength as a function of angle. Note that the azimuthal asymmetry (differences in intensity in $\phi$ direction) is more pronounced for larger particles. For 10$\mu$m particles (approximate size of nucleus, the largest organelle in most cells[12]), the scattering exhibits azimuthal asymmetry at $\theta$ ~178°, whereas with 2$\mu$m particle's (size of mitochondria), scattering is virtually $\phi$ independent at the same $\theta$.

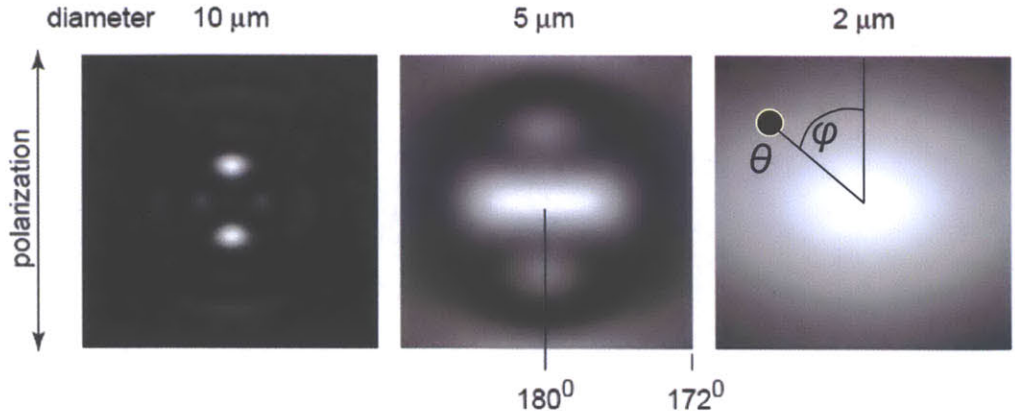


Figure 3.3: Scattering intensity maps (radial direction: $\theta$; angular direction: $\phi$) for $\theta = 180°$ (center of plot) to 172°, and $\phi = 0°$ to 360°. Results are calculated with $m = 1.05$ and $\lambda = 450$ nm.

Consider a collimated beam of linearly polarized light incident on an epithelial tissue. A small portion of this light is backscattered from the epithelial cell nuclei and smaller organelles, whereas the majority of the light is transmitted to deeper tissue layers, where it undergoes multiple scattering and becomes diffusive. The diffusive background is the diffuse reflectance that is not absorbed in the tissue and is collected at the surface. It should not depend on $\phi$ because its direction is randomized. However, SBS from epithelial organelles illuminated by the incident beam is $\phi$ dependent. Thus, we can measure single backscattering from epithelial organelles by measuring the $\phi$/LSS spectrum, $I_{\Delta\phi}(\lambda) = R_{\phi=0^\circ}(\lambda) - R_{\phi=90^\circ}(\lambda)$, where $R_{\phi=0^\circ}(\lambda)$ and $R_{\phi=90^\circ}(\lambda)$ are tissue reflectance spectra (consist of single and multiple scattering) with the same polarization measured at solid angles $\Omega_{\phi=0^\circ}$ and $\Omega_{\phi=90^\circ}$, which are centered at the same $\theta \sim 180°$ but at azimuthal angles $\phi = 0°$ and $\phi = 90°$, respectively. Since small particle SBS exhibits little $\phi$ asymmetry (figure 3.3), $I_{\Delta\phi}(\lambda)$ can be used to extract the SBS contribution specifically from epithelial cell nuclei.

$\phi$/LSS is sensitive to SBS from larger scatterers while P/LSS and SD/LSS measure all SBS. Since change in epithelial nuclear size is a hallmark of cancer[13], $\phi$/LSS can better focus on the signal of interest. This will likely reduce errors associated with the Mie theory and single particle scattering assumptions discussed in chapter 2. The technique relies on the $\phi$ independence of multiple scattering, which may not on average be valid for some few scattering events. We are developing a Monte-Carlo simulation that accounts for polarized light scattering to help analyze the performance of $\phi$/LSS. $\phi$/LSS can also be used to identify nuclear SBS while P/LSS or SD/LSS identifies backscattering from all organelles. Then, a scattering model such as Mie theory extrapolates the portion of $I_{ss,\,||}$ or $I_{SD}$ coming from nuclei. The remaining $I_{ss,\,||}$ or $I_{SD}$ is SBS from smaller organelles. This direction of research will not be discussed in this thesis. Section 3.4 explores the use of SD/LSS and $\phi$/LSS together in wide area imaging.

Research groups have studied light scattering from tissue by analyzing reflectance at different azimuthal angles. Kim et. al. developed an LSS instrument capable of measuring reflectance at three $\phi$ angles[14] and used azimuthal angle measurements in conjunction with P/LSS to study cancerous rat tissue. Popp et. al. studied light scattering dependence with both $\theta$ and $\phi$[15]. They found different tissue types can be classified by looking at azimuthal dependence of scattering.

### 3.4 Differential LSS imaging

SD/LSS and $\phi$/LSS show promise for removing diffuse background. The latter also isolates nuclear single backscattering. So far we have only discussed the application of these techniques for small area LSS diagnosis. This section expands the concepts to wide area imaging and discusses challenges involved in the transition.

Figure 3.2a depicted a square section of tissue surface illuminated by light except for a small circle in the middle, the dark spot. Consider the array of dark spots in figure 3.4. Each unit area is an independent diagnostic region like that in figure 3.2a. SD/LSS is conducted in each region by computing $I_{SD}$ (region) = $I_L$ (region) – $I_D$ (region). The SBS signal from each region is available, as in the imaging system of Gurjar et. al.

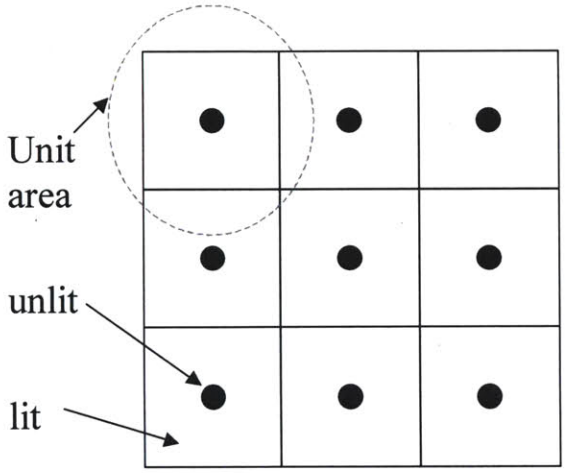


Figure 3.4: An array of dark spots each surrounded by a region (unit area) of illumination.

The array of figure 3.4 can cover several $cm^2$ to enable wide area imaging. This same configuration can conduct $\phi$/LSS using the illuminated area. First, we acquire two images of scattering at $\phi = 0°$ and 90°. This leads to two SD/LSS spectra, $I_{SD}$ (region, $\phi = 0°$) and $I_{SD}$ (region, $\phi = 90°$). At each region, the SBS spectra from large particles is $I_{\Delta\phi}$ (region) =

$I_{SD}$ (region, $\phi = 0°$) - $I_{SD}$ (region, $\phi = 90°$). Thus, in each region we can measure total SBS from all organelles and SBS specifically from nuclei.

Wide area imaging is important for cancer detection, but challenges not present in small area diagnosis must be addressed. Imaging requires a stronger illumination light source and faster data processing capabilities. Also, to conduct spectroscopy, images must be acquired at multiple illumination light wavelengths, as discussed in section 3.2. Taking multiple exposures increases the time required for diagnosis. A promising new method for conducting spectroscopic imaging with fewer exposures is under development. In chapter 4 we validate the assumptions of chapter 2 and the techniques of this chapter experimentally with tissue phantom and *ex vivo* tissue studies. At the same time, we encounter and address challenges with light scattering spectroscopy and imaging that are more fundamental and place limits on effectiveness.

---

[1] L. Perelman, V. Backman, G. Zonios, R. Manoharan, A. Nusrat, S. Shields, M. Seiler, C. Lima, T. Hamano, I. Itzkan, J. Van Dam, J. Crawford, M. Feld; "Observation of Periodic Fine Structure in Reflectance from Biological Tissue: A New Technique for Measuring Nuclear Size Distribution", Physical Review Letters; Vol. 80, No. 3, 627-30 (1998).

[2] J. Mourant, J. Freyer, H. Hielsher, A. Eick, D. Shen, T. Johnson; "Mechanisms of light scattering from biological cells relevant to noninvasive optical tissue diagnostics"; Applied Optics; Vol. 37, 3586-93 (1998).

[3] J. Wilson, T. Foster; "Mie theory interpretations of light scattering from intact cells"; Optics Letters; Vol. 30, No. 18, 2442-4 (2005).

[4] V. Backman; Reflectance Spectroscopy for Diagnosis of Precancerous Changes in Human Epithelium; Department of Physics, Massachusetts Institute of Technology (1996).

[5] H. van de Hulst; Light Scattering by Small Particles; Dover Publications, Inc. (1981).

[6] G. Zonios, L. Perelman, V. Backman, R. Manoharan, M. Fitzmaurice, J. Van Dam, M. Feld; "Diffuse reflectance spectroscopy of human adenomatous colon polyps *in vivo*"; Applied Optics, Vol. 38, No. 31, 6628-37 (1999).

[7] V. Backman, R. Gurjar, K. Badizadegan, I. Itzkan, R. Dasari, L. Perelman, M. Feld; "Polarized Light Scattering Spectroscopy for Quantitative Measurement of Epithelial Cellular Structures In Situ"; IEEE Journal of Selected Topics in Quantum Electronics; Vol. 5, No. 4, 1019-26 (1999).

[8] R. Gurjar, V. Backman, L. Perelman, I. Georgakoudi, K. Badizadegan, I. Itzkan, R. Dasari, M. Feld; "Imaging human epithelial properties with polarized light-scattering spectroscopy"; Nature Medicine; Vol. 7, No. 11, 1245-48 (2001).

[9] E. Hecht; Optics; Addison-Wesley (2002).

[10] D. Cuccia, F. Bevilacqua, A. Durkin, B. Tromberg; "Modulated imaging: quantitative analysis and tomography of turbid media in the spatial-frequency domain"; Optics Letters; Vol. 30, No. 11, 1354-6 (2005).

[11] M. Neil, R. Juskaitis, T. Wilson; "Method of obtaining optical sectioning by using structured light in a conventional microscope"; Optics Letters; Vol. 22, No. 24, 1905-7 (1997).

[12] V. Backman, V. Gopal, M. Kalashnikov, K. Badizadegan, R. Gurjar, A. Wax, I. Georgakoudi, M. Mueller, C. Boone, R. Dasari, M. Feld; "Measuring Cellular Structure at Submicrometer Scale With Light Scattering Spectroscopy"; IEEE Journal on Selected Topics in Quantum Electronics; Vol. 7, No. 6, 887-93 (2001).

[13] R. Cotran, V. Kumar, T. Collins; Pathologic Basis of Disease; W.B. Saunders Company (1999).

[14] Y. Kim, Y. Liu, R, Wali, H. Roy, M. Goldberg, A. Kromin, K. Chen, V. Backman; "Simultaneous Measurement of Angular and Spectral Properties of Lights scattering for Characterization of Tissue Microarchitecture and Its Alteration in Early Precancer"; IEE J. of Selected Topics in Quantum Electronics; Vol. 9 No. 2, 243-56 (2003).

[15] A. Popp, M. Valentine, P. Kaplan, D. Weitz; "Microscopic origin of light scattering in tissue"; Applied Optics; Vol. 42, No. 16, 2871-80 (2003).

# Chapter 4

# Implementation and experimental results

Chapter 3 introduced space differential (SD/LSS) and $\phi$-angle differential light scattering spectroscopy ($\phi$/LSS), two techniques capable of isolating single backscattering (SBS) from reflectance spectra dominated by multiple scattering. In this chapter, we take an experimental approach to evaluating the new techniques by using them to interrogate controlled tissue phantoms and *ex vivo* tissue samples. In the mean time, we develop instrumentation and inverse problem solutions that will soon lead to an *in vivo* spectroscopic imaging system based on light scattering spectroscopy (LSS) for clinical studies of cancer detection in cervix. Section 4.1 and 4.2 present $\phi$/LSS applied over a small area, $4mm^2$, to study tissue phantoms and colon tissue respectively. Section 4.3 uses a diffusion transport model to test the performance of SD/LSS and section 4.4 applies SD/LSS and $\phi$/LSS together in a wide area imaging modality to interrogate tissue phantoms.

## 4.1 $\phi$/LSS on tissue phantoms

In this section we present instrumentation for implementing $\phi$/LSS for small area diagnosis and conduct experiments on controlled tissue phantoms. A schematic diagram of the $\phi$/LSS experimental setup is shown in figure 4.1. Broadband white light from a xenon arc lamp (Oriel, Inc.) is color filtered (FWHM = 10nm) by a monochromator (Oriel, Inc.), and collimated by lens L1. The 4mm diameter opening of the mask is imaged 1:1 onto the sample by a 4f system (L2 and L3). Iris 1, placed one focal length

behind L2, restricts the divergence of the illumination light to a half angle of 0.5°. Light incident on the sample approaches at 30° from the normal to avoid measuring specular reflection, which can be much stronger then SBS in a small solid angle. Reflectance from the sample is redirected by a beamsplitter and imaged via a 4f system (L4 and L5) onto Iris 2, which selects the detection area to be the same as the illuminated area. Polarizers P1 and P2 ensure the polarizations of the collected and incident light are parallel. The CCD (Photometrics CoolSNAP HQ) is positioned at the focal plane of L6. As a result, reflectance from the sample at different angles is collected by different pixels of the CCD. Appendix C discusses how the optics in the instrument of figure 4.1 accomplish this. Reflectance from the sample is recorded at each incident light wavelength, which is stepped from 450nm to 700nm in 5nm increments (51 wavelength measurements). The recorded reflectance angular maps are similar to those of figure 3.3. The system has a maximum numerical aperture of 0.084, which corresponds to a scattering angle range of ±4.8° from direct backscattering.

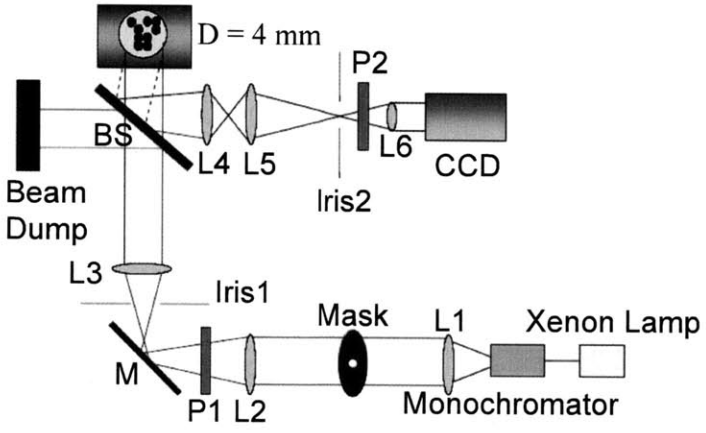


Figure 4.1: Small area $\phi$/LSS system.

Consider the reflectance angular map in figure 4.2. At each measurement wavelength we obtain one such map. Thus, every sample yields one set of 51 angular maps. Each experiment involves measuring reflectance from four samples to obtain four sets of maps. The first sample is the specimen of interest, such as *ex vivo* tissue. For the specimen we set exposure time to 10s to acquire each map. The time length is chosen to provide adequate signal to noise, which we will analyze later in Appendix B. The second sample is a diffuse reflectance normalization standard ($BaSO_4$) that is uniformly reflective across the visible wavelengths and reflects with a lambertian profile. Exposure time for the standard measurement is 5s. The third and fourth samples are neutral density filter (CVI Laser, LLC.) measurements taken with exposure times matching that of the first and second samples respectively. NDFs absorb the illumination light to account for stray light in the experiment room.

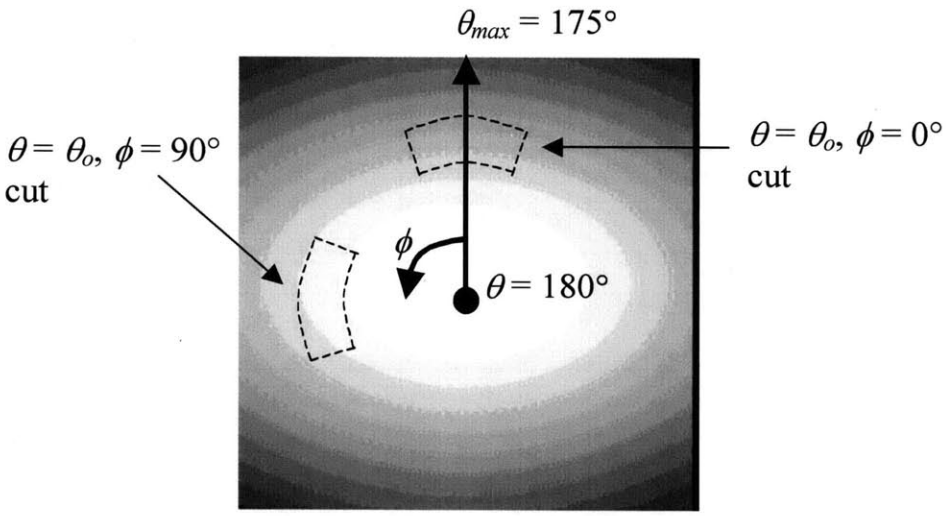


Figure 4.2: Data processing on each reflectance angular map.

For each angular map, we average the readings from CCD pixels within two "cuts", illustrated on figure 4.2. Each cut is centered about a target scattering angle $\theta_o$ and an

azimuthal angle, either $\phi = 0°$ or $\phi = 90°$. The extent of each cut spans $\pm 0.5°$ in $\theta$ and $\pm 10°$ in $\phi$. At $\theta_o = 178°$, each cut covers approximately 5000 pixels.

Denote the averaged reading in a cut as $C(\lambda, \theta, \phi)$. The $\phi$/LSS reflectance spectra are then:

$$R_{\phi=0} = \frac{C_{sample}(\phi = 0) - C_{NDF,sample}(\phi = 0)}{C_{\text{standard}}(\phi = 0) - C_{NDF,\text{standard}}(\phi = 0)}$$

$$R_{\phi=90} = \frac{C_{sample}(\phi = 90) - C_{NDF,sample}(\phi = 90)}{C_{\text{standard}}(\phi = 90) - C_{NDF,\text{standard}}(\phi = 90)}$$

We first subtract background readings from the specimen and standard measurements, then we divide the specimen reading by that of the standard. The latter accounts for any spectral and angular non-uniformities in the system because the standard is a spectrally and angularly uniform reflector. Note both spectra are dimensionless. With this method of data acquisition, $R_{\phi=0}(\lambda, \theta_o)$ and $R_{\phi=90}(\lambda, \theta_o)$ are spectra of reflectance averaged over the 4mm illumination spot.

We note an important subtlety in the instrument. The scattering angle measured by the instrument depends on the index of refraction of the medium because the angle of incidence of the illumination light is non-zero. Figure 4.3 shows scattering measured from a particle in medium.

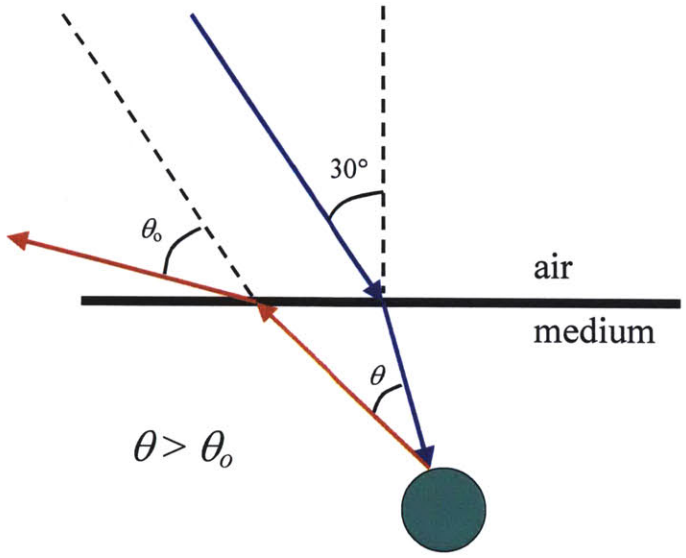


Figure 4.3: Scattering from a particle in medium. $\theta$ here indicates the scattering angle from direct backscattering. $\theta_o$ is the angle from direct backscattering (which is in the same direction as the incident light) measured by the instrument.

The difference occurs because air and medium have different indices of refraction. We can use Snell's law to find $\theta$ given $\theta_o$ if we know $n_{medium}$*. In the rest of this thesis, all references to $\theta$ imply the scattering angle in medium.

We use increasingly more complex tissue phantoms to establish the performance of the instrument, the assumptions of Mie theory and single particle scattering, and the technique $\phi$/LSS. The first step is to validate the instrument's abilities to accurately measure SBS. We prepare an optically thin sample of diameter $d$ = 10$\mu$m precision polystyrene spheres (Duke Scientific Inc.) immersed in a density matching $H_2O$ + glycerol solution. We match the density of the medium and the spheres to avoid non-ideal behavior caused by the spheres resting in contact with each other at the bottom of the

* The measurement of $\phi$ is also affected by the index of the medium, but the effect is small for scattering angles close to 180° and will be ignored in the rest of this thesis.

container. The scatterers in solution have relative index of refraction $m$ = 1.15. The container is a 1mm high, 1" inner diameter aluminum ring. This ring is placed on top of an absorptive NDF (CVI Laser, LLC.), the solution is poured into the resulting bowl, and the top is hermetically sealed by a high transmission window (CVI Laser, LLC). The concentration of the solution is set such that spheres cover approximately 10% of the 1" diameter area. This means the percentage of incident light scattered backwards is very small, much less than 10% because large particles predominantly scatter in the forward direction[1]. As a result, $R_{\phi=0}$ and $R_{\phi=90}$ will consist only of single scattering from homogeneous spheres spaced far apart and the system is well within the Mie theory and single particle assumptions.

Figure 4.4 shows $R_{\phi=0}$ ($\theta$ = 178°), $R_{\phi=90}$ ($\theta$ = 178°), and $I_{\Delta\phi}$ ($\theta$ = 178°) measured from the spheres solution. To check the accuracy of the system, we use Mie theory to compute the correct $I_{\Delta\phi}$ ($\theta$ = 178°) using the manufacturer's specifications of $d$ = 9.964$\mu$m ± 0.058$\mu$m and index of refraction of the spheres. We account for variation of index of refraction with wavelength in water and polystyrene, but we only have $n_{glycerol}$ = 1.474 at 589nm[2]. The Mie theory spectrum is also plotted in figure 4.4. The agreement is excellent. These results show the system can accurately measure SBS.

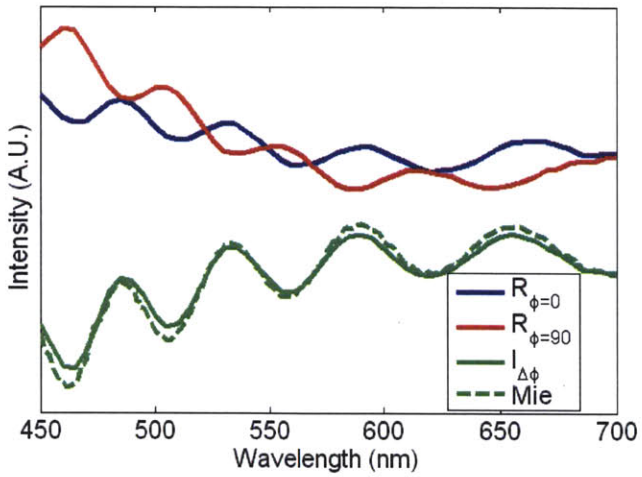


Figure 4.4: $R_{\phi=0}$, $R_{\phi=90}$, and $I_{\Delta\phi}$ measured from the spheres solution at $\theta = 178°$. The dotted green spectrum is $I_{\Delta\phi}$ computed with Mie theory. The spectral linewidth (10nm FWHM) of our monochromator is accounted for in the computation. We divide $R_{\phi=0}$ and $R_{\phi=90}$ by their respective means prior to subtraction. The computed spectrum is also divided by its mean to compare with the data.

With instrument accuracy validated, we next test the ability of $\phi$/LSS to isolate SBS from large scatterers near the surface (epithelial nuclei) in the presence of smaller scatterers also near the surface (smaller organelles) and diffuse background (underlying tissue and blood). The tissue phantom for this study is illustrated in figure 4.5 and follows the tissue model of chapter 2. The top layer, which simulates the epithelium, is a mixture of 10$\mu$m (Duke Scientific) and 1$\mu$m (Polysciences Inc.) diameter spheres, representing nuclei and mitochondria, respectively, suspended in a water-glycerol mixture. The bottom layer, which simulates the underlying tissue, consists of a 2% Intralipid (Fesenius Kabi Clayton, L.P.) solution mixed with approximately 5 mg/mL hemoglobin $A_0$ (Sigma-Aldrich) to provide physiologically relevant diffusive reflectance and absorption.

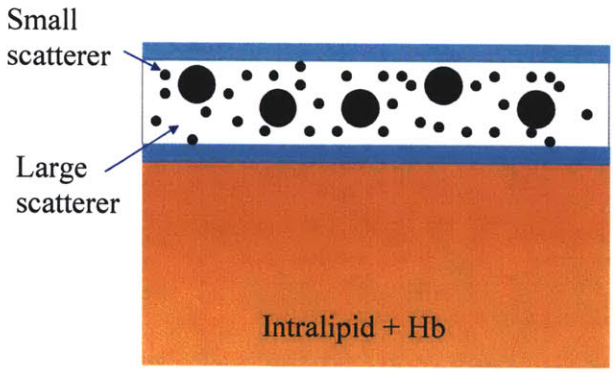


Figure 4.5: Two-layer tissue phantom. The medium in the 1mm thick top layer is a density matching glycerol + water solution. High transmission windows separate the top layer from air and from the lower layer, which is deep enough to appear infinite. The area coverage of 10$\mu$m spheres is approximately 10% of the sample's cross-sectional area. The number of 1$\mu$m spheres is varied.

We measure reflectance spectra $R_{\phi=0^\circ}(\lambda)$ (figure 4.6a) and $R_{\phi=90^\circ}(\lambda)$ at $\theta = 178^\circ$, with the ratio between the number of 1 and 10$\mu$m spheres (see legend) varied to span the range of ratios between the number of mitochondria and nuclei in human cells. The results show that even without 1$\mu$m spheres, the diffusive background overwhelms the SBS intensity spectrum (the inset of figure 4.6a), which is the blue curve of figure 4.4. When 1$\mu$m spheres are added, the reflectance signal size decreases with increasing number of 1$\mu$m spheres. This is because the light delivered to the 10$\mu$m spheres and the lower layer is attenuated by scattering from the many 1$\mu$m spheres in the top layer. These measured results demonstrate that the signal contributed by other scatterers and absorbers can significantly mask SBS from the 10$\mu$m spheres if we only look at $R_{\phi=0}$.

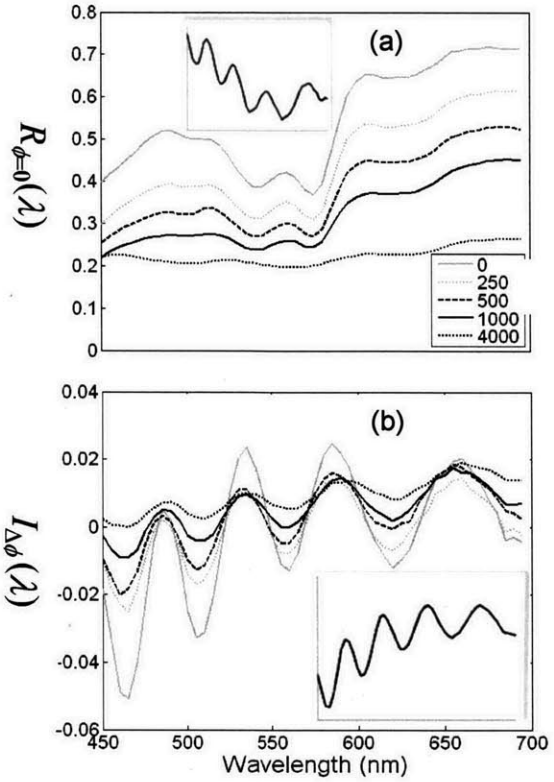


Figure 4.6: (a) $R_{\phi=0^\circ}(\lambda)$ and (b) $I_{\Delta\phi}(\lambda)$ for two-layer phantoms with varying number of 1$\mu$m spheres measured at $\theta$ = 178°. The legend shows the ratio between the number of 1$\mu$m spheres and 10$\mu$m sphere. The irradiance axes are in arbitrary units. The insets of (a) and (b) are the blue and green curves of figure 4.4 and show pure SBS spectra from 10$\mu$m spheres only.

We then take the difference between $R_{\phi=0^\circ}(\lambda)$ and $R_{\phi=90^\circ}(\lambda)$ to obtain $I_{\Delta\phi}(\lambda)$ (figure 4.6b). We compare $I_{\Delta\phi}(\lambda)$ measured from 10$\mu$m spheres in the presence of other scatterers and absorbers to $I_{\Delta\phi}(\lambda)$ measured from 10$\mu$m spheres alone (see the inset of figure 4.6b). The latter is the green curve of figure 4.4. The results show that the oscillatory features are preserved under all conditions tested. We note that the contrast of the oscillatory component decreases as the density of 1$\mu$m spheres is increased. This occurs because the SBS azimuthal asymmetry is $\theta$ dependent, and the incident light needs

to be collimated and polarized to define $\theta$ and $\phi$ (section 2.1). The forward scattering from 1$\mu$m spheres partially decollimates and depolarizes the light incident on the 10$\mu$m spheres. Consequently, the SBS azimuthal asymmetry from 10$\mu$m spheres is reduced.

These results show $\phi$/LSS helps to identify the single backscattering signal from larger scatterers, but the single particle scattering approximation of chapter 2 may not be well satisfied because scattering from 1$\mu$m spheres affects single backscattering from the 10$\mu$m spheres. However, this may not significantly affect the accuracy with which we can solve the inverse scattering problem to identify the size and index of refraction of large scatterers in the sample. We observe that if we subtract flat spectra, such as the mean of each spectra, from the respective $I_{\Delta\phi}(\lambda)$'s of figure 4.6b, we are left with spectra of similar slope and oscillation frequency. Only the amplitude of the features vary (figure 4.7).

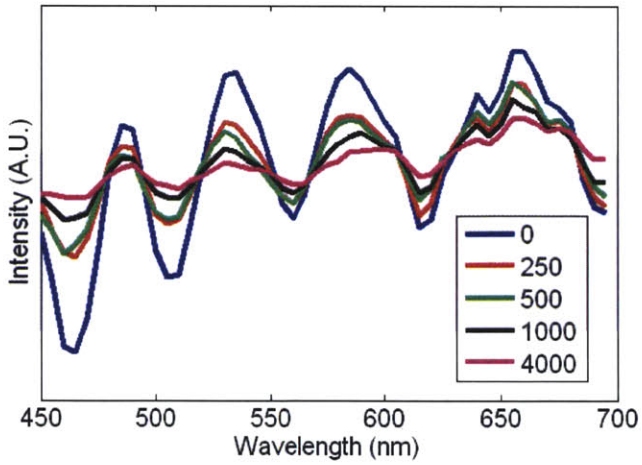


Figure 4.7: $I_{\Delta\phi}$ for 10$\mu$m spheres measured with the system of figure 4.1. All spectra have been mean subtracted.

This similarity between the spectra despite vastly different amounts of small particles suggests we may be able to use the single particle scattering approximation to solve the inverse scattering problem.

Previously, we used the manufacturer's specifications for the spheres to validate assumptions and techniques. In samples where we do not know the size and index of refraction of scatterers, we need to solve the inverse scattering problem. This can be accomplished with our assumptions of Mie and single particle scattering. We use Mie theory to compute $I_{\Delta\phi}(\lambda, d, m, \theta)$ for $\lambda$ from 450 – 700nm in increments of 5nm, $\theta$ from 177° – 180° in increments of 0.1°, and ranges of physiologically relevant $d$ and m. The finite sized solid angles of collection defined by the cuts of figure 4.2 are accounted for in these calculations by integrating the differential scattering cross-sections over the solid angle. We then find the combination of parameters that minimizes the least square error between experiment and theory (fitting):

$$\begin{aligned} &\min_{N,d,m,\theta}\left(\sum_{j=1}^{51}\left(I_{\Delta\phi}^{\exp}(\lambda_j)-I_{\Delta\phi}^{0}(\lambda_j)\right)^2\right) \\ &I_{\Delta\phi}^{0}=\sum_i N_i I_{\Delta\phi}^{Mie}(d_i,m,\theta) \end{aligned} \tag{4.1}$$

*Mie* and exp indicate Mie theory computed spectrum and measured spectrum respectively. The subscript $j$ identifies the 51 wavelength measurements. The subscript $i$ in $N_i$ indicates the number of particles of diameter $d_i$. Since our data is measured in dimensionless units, $N_i$ describes the amount of one size of particle versus the amount of another size. This fitting routine assumes a constant index of refraction for all sizes of scatterers. Readers may wonder why it is necessary to search scattering angle when the

position of the cut in figure 4.2 should indicate $\theta$. Recall from the discussion of figure 4.3 that because the scattering medium and air have different index of refractions, $\theta$ cannot be exactly determined unless $n_{medium}$ was known, which is not generally possible in tissue. With this formulation, we can extract from the measured spectrum $n_i$ $(d_i)$ = $N_i$ (size distribution), $m$ (index of refraction), and $\theta$.

Equation 4.1 will be non-unique if the number of diameters $d_i$ is too much greater then the number of wavelength measurements because $d_i$'s are free parameters and $\lambda$'s are constraints*. Since we are limited to 51 wavelengths (450 – 700nm in increments of 5nm), we can either have sparse coverage of the diameter range, or assume a functional form for $n_i$. In this thesis we follow the approach of Gurjar et. al.[3] and Backman et. al.[4], which assumes the size distribution takes the form of a Gaussian probability density function:

$$n_i(d_i) = \frac{N_0}{\sigma\sqrt{2\pi}} e^{-(d_i - d_m)^2/(2\sigma^2)}$$

The free parameters are now $N_0$, the amplitude of the distribution representing the total number of particles**, $d_m$ the mean diameter, $m$ the representative relative index of refraction, and $\sigma$, the spread of diameters. Many distributions in nature have a Gaussian profile and this assumption still enables LSS to detect average nuclear enlargement and

* The wavelength measurements and diameters are close together, so they are not fully independent constraints and free parameters. We do not consider this in the analysis.

** Like $N_i$ discussed earlier, $N_0$ is dimensionless. A larger $N_0$ indicates more particles in the sample underwent backscattering events and vice versa. We will use spheres samples to calibrate $N_0$ outputs in later experiments.

hyperchromatism. We also assume $n_{medium}$ = 1.35, based on the findings of previous researchers[5], so we can focus on one scattering angle.

With equation 4.1 and the assumptions on size distribution and medium index of refraction, we attempt to extract $N_0$, $d_m$, $\sigma$, and $m$ from the spectra of figure 4.6b to test the effectiveness of $\phi$/LSS. To make the experiment and theory parts of equation 4.1 comparable, we subtract the respective means (in wavelength) from both spectra, similar to the process of figure 4.7, then normalize the remainders by the respective absolute areas under each spectrum. The area under the data spectrum divided by that of the fit is $N_0$. This normalization is specified in equation 4.2.

$$
\begin{aligned}
I_{\Delta\phi}^{normalized} &= \frac{num}{\sum_{i=1}^{51}\left|num(\lambda_i)\right|} \\
num &= I_{\Delta\phi} - mean\left(I_{\Delta\phi}\right) \\
N_0 &= \frac{\sum_{i=1}^{51}\left|num_{\exp}(\lambda_i)\right|}{\sum_{i=1}^{51}\left|num_{Mie}(\lambda_i)\right|}
\end{aligned}
\tag{4.2}
$$

The subscripts exp and *Mie* indicate experiment and Mie theory spectra respectively. Mean is taken over the 51 wavelength measurements. $I_{\Delta\phi}^{normalized}$ is computed for data and fit spectra. The normalization accounts for the attenuation of oscillatory feature amplitudes by small particles. Equation 4.1 will extract the optimum $N_0$, $d_m$, $\sigma$, and $m$ combination using spectral features only, such as the oscillatory components in figure 4.6b. In table 4.1, we present solutions to the inverse problem when $d_m$ is allowed to vary from 8 - 12$\mu$m in 0.005$\mu$m increments, $m$ from 1.15 – 1.2 in 0.001 increments, and σ

from 0.01 - 0.3$\mu$m in 0.01$\mu$m increments. Note this range of $d_m$ means the Mie theory portion of equation 4.1 will not account for SBS from the 1$\mu$m spheres, so this inversion tests the ability of $\phi$/LSS to identify SBS specifically from the large scatterers.

Table 4.1: Scatterer parameters extracted with equation 4.1 from the $I_{\Delta\phi}(\lambda)$'s measured from two-layer phantoms (figure 4.6b). Ratio is the ratio of 1 to 10$\mu$m spheres in the phantom. The manufacturer specifications are provided for the 10$\mu$m spheres.

| | $d_m$ ($\mu$m) | $\sigma$($\mu$m) | $m$ |
|---|---|---|---|
| **Manufacturer specifications for 10$\mu$m spheres** | 9.964 | 0.06 | 1.176 |
| | | | |
| **Ratio = 0** | 9.915 | 0.01 | 1.173 |
| **Ratio = 250** | 10.125 | 0.01 | 1.185 |
| **Ratio = 500** | 10.110 | 0.02 | 1.185 |
| **Ratio = 1000** | 10.15 | 0.07 | 1.186 |
| **Ratio = 4000** | 10.500 | 0.27 | 1.189 |

We observe from table 4.1 that even in the presence of diffuse background and absorption and with 1$\mu$m particles outnumbering 10$\mu$m particles 4000 to 1, the errors in extracted values of $d_m$ and $m$ never deviate by more than 10% from the manufacturer's specifications. These experiments clearly demonstrate that $\phi$/LSS can detect azimuthal asymmetry in reflectance and accurately measure mean size and index of refraction in tissue-like conditions. However, the Mie fitting does not measure $\sigma$ as accurately. From our data, the single particle scattering assumption's limits appear as inaccuracies in the spread of diameters. Increasing $\sigma$ reduces the amplitude of oscillatory features, which is what we observe in the data. When we study *ex vivo* tissue in section 4.2, we can expect accurate results for $d_m$ and $m$.

### 4.2 $\phi$/LSS on *ex vivo* colon tissue

Section 4.1 demonstrated the $\phi$/LSS instrument and presented the data acquisition procedures. It also presented the inverse light scattering solution based on Mie theory and the single particle approximations. In this section, we use the system and the fitting routine to study cancerous and normal colon tissue *ex vivo*. At the same time, the tissue samples in this preliminary study help to set the fitting routine. Future experiments on more *ex vivo* tissue will test the robustness of the algorithm and $\phi$/LSS. The results of this section have been submitted for publication in Physical Review Letters.

We obtain samples of normal and cancerous colon tissue from excess/discarded materials removed during surgery at the Massachusetts General Hospital (MGH). This study was approved by the Institutional Review Board of MGH and the Committee on Use of Humans as Experimental Subjects of MIT. Samples are transported to the lab in a physiological buffer (Hanks Balanced Salts Solution) and kept at 4 °C until use. Spectra are collected at room temperature within 6 hours of tissue excision. After data acquisition, samples are fixed in 10% neutral buffered formalin and embedded in paraffin. Five micron thick sections are cut and stained with hematoxylin and eosin for pathological diagnosis and nuclear morphometry (measure size and shape). The sections are placed between two glass coverslips for viewing under a microscope. To conduct nuclear morphometry of the histological sections, for each section we select at least 100 surface epithelial nuclei from 5 randomly selected fields viewed with a 100x objective on an Olympus BX41 microscope equipped with a QImaging Micropublisher 5.0 camera. Epithelial nuclei with a well-defined nuclear contour in the plane of the image are selected using Photoshop and Fovea Pro 3.0 segmentation tools. A binary image of the

segmented nucleus is constructed for feature analysis using Fovea Pro. From this image, we extract size and shape information on the nucleus. In this thesis we will utilize two parameters of nuclear shape and size, $D_M$ and $L_M$. For each nucleus, we find the diameter of the circle with the same area and also the longer axis of the rectangle that best fits the nucleus' dimensions*. $D_M$ is the diameter of the circle. $L_M$ is the length of the longer axis of the rectangle.

We use the instrument of figure 4.1 to measure reflectance from the tissue samples. The resulting $I_{\Delta\phi}(\lambda)$ spectra are fitted to Mie theory to extract $d_m$ and $m$ from the samples. For *ex vivo* tissue, we compute $I_{\Delta\phi}(\lambda)$ spectra using Mie theory with $d_m$ spanning 0.1 - 25$\mu$m in 0.1$\mu$m increments, $m$ from 1.03 – 1.08 in 0.005 increments, and $\sigma$ from 0.1 - 3$\mu$m in 0.1$\mu$m increments. These ranges correspond to physiologically relevant nuclear size and index of refraction variations [6]. We have included more sizes and indices then recommended by the literature in case $\phi$/LSS obtains a good fit for values slightly beyond the published ranges. These pre-computed spectra will be used by the fitting routine. In section 4.1 we saw that a large ratio of small to large scatterers causes errors in $\phi$/LSS's measurement of $\sigma$. We also expect some errors when measuring this on *ex vivo* tissue because smaller organelles such as mitochondria can influence scattering from nuclei. Therefore, we take physically reasonable steps to de-emphasize $\sigma$ in equation 4.1 by using extra information from our knowledge of tissue structure and light scattering. This will increase the uniqueness of the extracted $d_m$ and $m$ because we reduce the number of free parameters. Below is a step-by-step description of the fitting

* Refer to Fovea Pro's manual for how a rectangle is fitted to an arbitrarily shaped 2D object.

algorithm to solve the inverse scattering problem in *ex vivo* tissue studies. The matlab coding is in Appendix A. This algorithm will be "trained", using the terminology of neural networks, to distinguish spectra measured from normal and cancerous samples in this study.

Step 1: We discussed in chapter 2 that azimuthal asymmetry varies with scattering angle and wavelength. For large particles, the change is greater. We compute the asymmetry parameter of the difference between the two measured spectra $I_{\Delta\phi}(\theta = 178°)$ and $I_{\Delta\phi}(\theta = 179°)$:

$$AP = AP_{DC} + AP_{amp} + AP_{slope}$$

$$AP_{DC} = A * \left| mean\left(I_{\Delta\phi}(\theta = 178°)\right) - mean\left(I_{\Delta\phi}(\theta = 179°)\right) \right|$$

$$AP_{amp} = B * \sqrt{\sum_{i=1}^{51} \left(I_{\Delta\phi}(\theta = 178°, \lambda_i) - I_{\Delta\phi}(\theta = 179°, \lambda_i)\right)^2}$$

$$AP_{slope} = C * \sqrt{\sum_{i=1}^{51} \left( \frac{\partial}{\partial \lambda_i}\left(I_{\Delta\phi}(\theta = 178°, \lambda_i)\right) - \frac{\partial}{\partial \lambda_i}\left(I_{\Delta\phi}(\theta = 179°, \lambda_i)\right) \right)^2}$$

AP quantifies change in azimuthal asymmetry with angle and wavelength. If AP is greater then a cutoff value*, scattering from the tissue sample is dominated by large particles (cancerous), else, scattering is dominated by small particles (normal). Large and small particles have different $d_m$ ranges, which we will set to best separate the normal and cancerous samples in this study.

* This value is adjusted to provide the best sensitivity and specificity from the samples available in this study.

Step 2: Compute the fitting using $I_{\Delta\phi}$ ($\theta$ = 178°). Vary $m$ from 1.03 – 1.08 in 0.005 increments. For each index, vary $d_m$ over the range determined in step 1. For each $m$ and each $d_m$, vary $\sigma$ from 5% to 10% of the current $d_m$ in 1% increments. In computer coding, these instructions are a set of nested loops. In each stage of the loop, compute the least square error between Mie theory prediction and measurement as in equation 4.1.

Step 3: In each loop stage of step 2, compute the amplitude of the Gaussian, determined by the current values of $d_m$ and $\sigma$, required to best fit the data:

$$N_o = \frac{\sum_{i=1}^{51} \left| num_{\exp}(\lambda_i) \right|}{\sum_{i=1}^{51} \left| num_{Mie}(\lambda_i) \right|}$$

$$num = I_{\Delta\phi} - mean\left(I_{\Delta\phi}\right)$$

We use $N_o$ with data from the spheres experiments of figure 4.4 to estimate the total number of scatterers in the illuminated area and the fractional area coverage of the scatterers in the sample. In the phantom experiment, we knew the number of scatterers $N$, their parameters $d_m$, $m$, and $\sigma$, the resulting CCD readings at each wavelength, and the predictions of Mie theory. This allows us to estimate the $N$ observed in the tissue sample. Refer to the program in Appendix A for more details. The area coverage (CA) is then approximately 0.25 $\pi$ $d_m^2$ $N$ divided by the area of the illumination (4mm diameter circle). We use CA as a constraint. If the CA of any set of fitting parameters falls outside of physical bounds, the current loop of $d_m$, $m$, and $\sigma$ is not feasible. We expect an upper bound of approximately 1 because a measured CA = 1 means the measured sample area is completely covered by one layer of scatterers. The lower bound cannot be much lower

then CA = 0.028 if we assume the cell configuration in figure 4.8. This is because CA = 0.028 will correspond to backscattering from one layer of cells with the configuration of figure 4.8. If multiple cell layers contribute to SBS, the area coverage will be greater. We set a constraint $0.05 < CA < 1.0$.

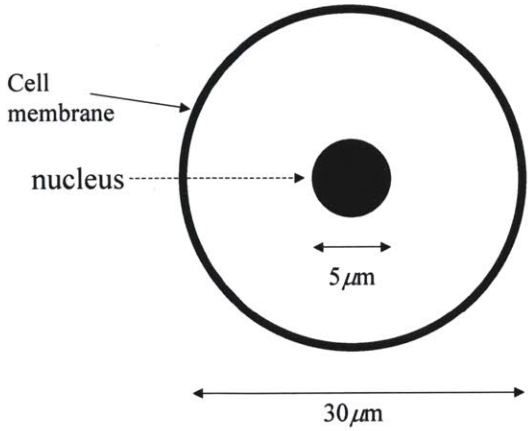


Figure 4.8: If we assume the cell is approximately 30μm in diameter and the nucleus is no smaller than 5μm in diameter, the fraction of the total area covered by the nuclei in one layer of cells, such as the most superficial of epithelial cells, is approximately $(2.5\mu m)^2 / (15\mu m)^2$.

Step 4: Use $N_0$, $d_m$, $m$, and $\sigma$ to compute the SBS spectrum at $\theta = 178°$, $\phi = 0°$, $I_{\phi=0}(\lambda)$. If the Mie theory and single particle scattering approximations are fully satisfied by SBS from colon tissue, $I_{\phi=0}(\lambda) < R_{\phi=0}(\lambda)$ at all wavelengths. Since the tissue phantom studies demonstrated the single particle scattering approximation is not fully satisfied, we relax the constraint slightly to $I_{\phi=0}(\lambda) < k*R_{\phi=0}(\lambda)$, where k may be greater than 1. Any combination of scatterer parameters that violates this constraint is not feasible. k will be determined with the training set later in this section.

Step 5: Of the feasible combinations of parameters $N$, $d_m$, $m$, and $\sigma$, the set with the lowest least square error after step 4 is the inverse scattering solution.

The constraints of the fitting algorithm along with the ranges of $d_m$ and $m$ put physical restrictions on the solution. Without these constraints, equation 4.1 produces multiple solutions that seem to agree equally well with the data. The constraints are set by training the algorithm with the first set of data. For this preliminary study, we analyzed four colon cancers from four patients and eight normal colon epitheliums from the four cancer patients and three additional cancer-free patients. In total, 7 cancers and 10 normal samples were measured with the instrument, but data from 3 cancers were discarded because upon analyzing the histology sections, we found they had thick layers of necrotic material (dead cells) covering the epithelium. As a result, the instrument cannot measure SBS from the epithelial nuclei. This limitation does not significantly affect the diagnostic abilities of the system because those samples were not early stage epithelial cancers. Two normal samples were not analyzed because their measured $I_{\Delta\phi}$ had features of hemoglobin absorption, which affects the fitting routine. This residual indicates either $\phi$/LSS did not effectively isolate SBS for these samples or there was blood on the surface of the tissue. For the 12 suitable samples, we measured $I_{\Delta\phi}(\lambda)$ from each. Figure 4.9 plots one normal and one cancerous spectrum, along with their Mie theory fits. The azimuthal asymmetry is more pronounced in cancerous tissue as expected. In appendix B we discuss a signal to noise analysis of the $I_{\Delta\phi}$ spectra to insure the signal is sufficiently beyond random noise.

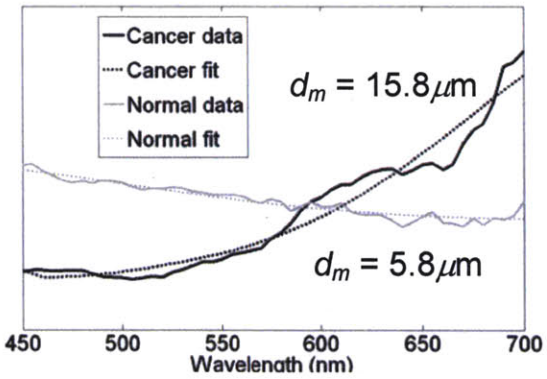


Figure 4.9: $I_{\Delta\phi}(\lambda)$ measured at $\theta$= 178° from two colon tissue samples.

From these 12 samples, we found a set of constraint limits that distinguished between $d_m$ measured from cancerous and normal samples. In step 1, we set the cutoff value of AP to 0.004. This number is unique to this instrument but it can be rescaled for use with another instrument based on $\phi$/LSS. For large and small scatterers in step 1, we allow $d_m$ to range from 9 - 25$\mu$m and 5 – 11$\mu$m respectively. A, B, and C are set to 0.05, 0.0093, and 0.475 respectively. The k factor in the constraint of step 4 is set to 2. With these constraint limits, we obtain the results in table 4.2. $d_m$ and $m$ are the most important parameters because the tissue phantom studies in section 4.1 validated their accuracy.

Table 4.2: Scatterer parameters extracted from 12 colon tissue samples.

| | **$\phi$/LSS Parameters** | | |
|---|---|---|---|
| **Sample** | ***N*** | ***$d_m$ ($\mu$m)*** | ***m*** |
| Cancer 1 | 270000 | 15.8 | 1.055 |
| Cancer 2 | 54000 | 21.8 | 1.065 |
| Cancer 3 | 57000 | 20.4 | 1.065 |
| Cancer 4 | 170000 | 22.5 | 1.050 |
| Normal 1 | 8900000 | 5.8 | 1.05 |
| Normal 2 | 770000 | 7.7 | 1.06 |
| Normal 3 | 3900000 | 6.7 | 1.06 |

| | | | |
|---|---|---|---|
| Normal 4 | 510000 | 9.4 | 1.06 |
| Normal 5 | 3000000 | 8.5 | 1.05 |
| Normal 6 | 810000 | 9.3 | 1.06 |
| Normal 7 | 1400000 | 9.3 | 1.06 |
| Normal 8 | 1000000 | 9.4 | 1.06 |

There is a clear distinction between nuclear size in normal and cancer samples when using $d_m$. For normal tissue, $d_m$ is consistent with $D_M$. However, all the $d_m$ measured from cancerous tissue lie outside the $D_M$ size distribution (figure 4.10a). Consequently, the separation between cancerous and normal tissue is much more pronounced when $d_m$, instead of $D_M$, is used. While this is favorable in terms of cancer detection using $\phi$/LSS, the physical origin of this discrepancy needs to be addressed. We note that a deviation between $D_M$ and $d_m$ is expected for elongated epithelial cell nuclei. Therefore, we consider the non-spherical shape of each nucleus by comparing $d_m$ to $L_M$ (figure 4.10b). We find $d_m$ is still consistent with $L_M$ for normal tissue. Interestingly, unlike the results comparing $d_m$ and $D_M$, all cancerous $d_m$ are inside of the $L_M$ size distribution. These findings suggest that $d_m$, the particle "diameter" measured with $\phi$/LSS, is consistent with the longest dimension of the aspherical nucleus. The effects of aspherical shape on $\phi$/LSS are under investigation both theoretically and experimentally. The sensitivity and specificity of using $\phi$/LSS and the fitting routine for cancer detection will be assessed in a much larger study of *ex vivo* tissue.

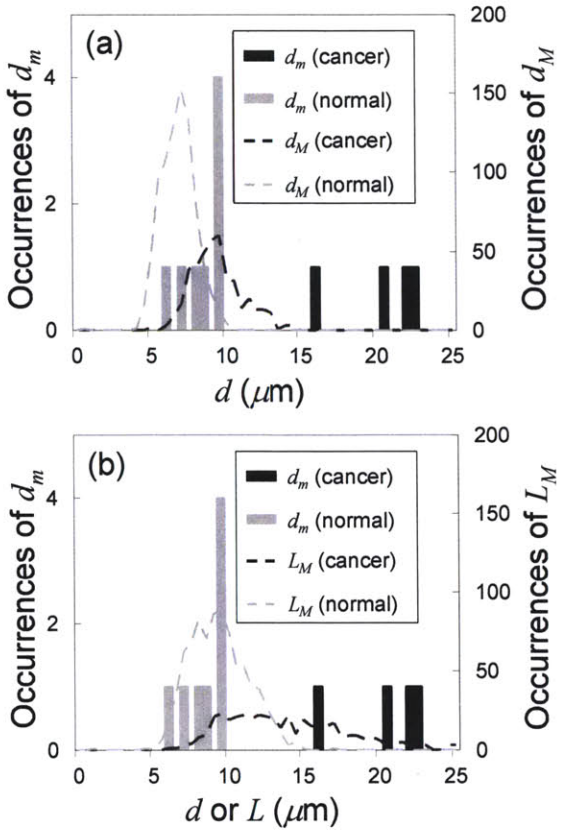


Figure 4.10: (a) Histograms of $d_m$ and $D_M$ (defined in text). (b): Histograms of $d_m$ and $L_M$ (defined in text). The y-axes indicate the number of occurrences of each size. For morphometry results, the measured $D_M$ and $L_M$ from all samples are binned in 0.5$\mu$m units. For $\phi$/LSS results, the 12 extracted $d_m$ are binned in 0.5$\mu$m units.

### 4.3 SD/LSS effectiveness

In this section, we assess the effectiveness of SD/LSS at removing multiple scattering and diffuse reflectance from reflectance spectra using a mathematical model and numerical simulations. To estimate the multiple scattering residual left in $I_{SD}$, we use the diffusion model of light propagation developed by Farrell et. al.[7] with tissue levels of scattering and absorption. Farrell et. al.'s model computes the amount of light returning to the surface a distance $r$ away from a point source illumination, assuming diffusion (all scattering events are isotropic in angle), unpolarized light, and a homogeneous tissue.

Due to the assumptions, all returned light is diffuse reflectance. If we study the difference in amount of light returned from a simulated sample with and without using SD/LSS, we obtain an estimate of the effectiveness of SD/LSS at accounting for light returning from lower tissue layers like that modeled in figure 2.1.

We numerically integrate Farrell et. al.'s equation with the light delivery geometry of figure 3.2a, as written by Zonios et. al.[8] The equation is then integrated over the collection geometry. To model diffuse reflectance collected by the dark spot $I_{Dark}$, the collection geometry is the dark spot in figure 3.2a (using SD/LSS). To model the correct amount of diffuse reflectance $I_{Light}$, we set the collection geometry to be a circle the size of the dark spot but completely in illuminated area (no SD/LSS). No dark spot is present. $I_{Light}$ and $I_{Dark}$ allow us to compare the correct amount of diffuse reflectance versus the amount actually collected by the dark spot due to its finite size. Table 4.3 shows $I_{Dark}$ / $I_{Light}$. The value is the approximate fraction of multiple scattering accounted for by SD/LSS with the given dark spot size. Smaller dark spots enable SD/LSS to more effectively isolate SBS.

Table 4.3: Irradiance returned from dark spot divided by irradiance from illuminated area of the same size. The value is averaged over wavelength. The width of the illuminated box is 1mm.

| ***Radius of dark spot (mm)*** | **0.2** | **0.1** | **0.05** | **0.01** |
|---|---|---|---|---|
| $I_D / I_L$ | 0.735 | 0.928 | 0.982 | 0.999 |

SD/LSS and P/LSS both remove diffuse background to isolate single backscattering. We are developing a Monte-Carlo simulation, which accounts for polarized light, of multiple Mie scatterings in tissue that can estimate the performance of

P/LSS, $\phi$/LSS, and SD/LSS. The Monte-Carlo simulation program is an important development tool. Based on preliminary estimates with Farrell et. al's diffusion model, SD/LSS with a 50$\mu$m dark spot can remove approximately 98% of multiple scattering. We note from the discussion of chapter 3 that dark spot size cannot be made infinitesimally small because an imaging system must be able to resolve the difference between illuminated and non-illuminated areas of the sample.

### 4.4 Spectroscopic imaging with SD/LSS and $\phi$/LSS

In section 4.1, we validated $\phi$/LSS and our approximations of Mie theory and single particle scattering with tissue phantoms. In section 4.2, we studied *ex vivo* colon tissue and developed an algorithm to solve the inverse scattering problem and extract the size of the nuclei given the measured $\phi$/LSS spectra. In this section, we calibrate an instrument, which will be used to test the imaging concepts of section 3.3, with $d = 10\mu$m spheres.

Figure 4.11 shows the instrument we use to project the dark spots array of figure 3.4 onto the sample. This instrument is a modification of the instrument presented in figure 4.1. The mask has the pattern of figure 3.4. Each unit area is a 1mm square and each dark spot is 0.5mm in diameter. The collection lenses L4 and L5 image the illuminated area of the sample onto the CCD. Iris 2 is placed at the focal planes of L4 and L5 to select the scattering ($\theta$) and azimuthal ($\phi$) angles permitted to pass (refer to Appendix C). With this configuration, the CCD will record an image of the sample surface with only light that has scattered within the range of $\theta$'s and $\phi$'s permitted by

Iris2. Iris2 is a circular opening that permits approximately ±0.5° in $\theta$ and ±11° in $\phi$ to pass. This opening yields a minimum dark spot radius, due to diffraction, of approximately 60$\mu$m.

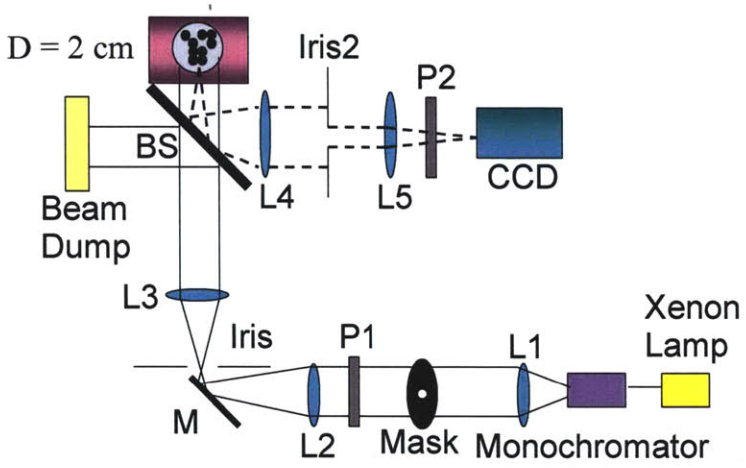


Figure 4.11: LSS imaging system. The symbols have the same meaning as those in figure 4.1.

We choose the scattering angle measured by rotating the beamsplitter. We then choose the azimuthal angle, $\phi = 0°$ or $\phi = 90°$, by having the polarizers P1 and P2 aligned to pass polarizations parallel (horizontally polarized) and perpendicular (vertically polarized) to the scattering plane. Moving the beamsplitter and the polarizers instead of Iris 2 keeps the optical path traveling through the center of the lenses and minimizes spherical aberration.

To acquire reflectance spectra, we take measurements of the specimen of interest and a $BaSO_4$ diffuse reflectance standard (refer to section 4.1). For imaging, we do not require room light measurements because the illuminated and dark areas of each region both contain the same amount of room light. When $I_{SD}$ is computed, room light will be removed. For each sample, two images are taken, one with the polarizers horizontal ($\phi =$

0°) and another with the polarizers vertical ($\phi = 90°$). At each region, the reflectance from the illuminated and non-illuminated areas are:

$$R_L = \frac{C^{sample}_{illu\,\min ated}}{C^{s\tan dard}_{illu\,\min ated} - C^{s\tan dard}_{non-illu\,\min ated,0}}$$

$$R_D = \frac{C^{sample}_{non-illu\,\min ated}}{C^{s\tan dard}_{illu\,\min ated,0} - C^{s\tan dard}_{non-illu\,\min ated,0}}$$

$C$ is the average CCD reading from all illuminated or non-illuminated pixels in the region. $C^{s\tan dard}_{illu\,\min ated,0}$ and $C^{s\tan dard}_{non-illu\,\min ated,0}$ are the averages of $C^{s\tan dard}_{illu\,\min ated}$ and $C^{s\tan dard}_{non-illu\,\min ated}$ over all illuminated/non-illuminated pixels in the region respectively. To obtain the SD/LSS spectra, we compute $I_{SD}$ (region, $\phi$) = $R_L$ (region, $\phi$) – $R_D$ (region, $\phi$) as in chapter 3. The $\phi$/LSS spectra are $I_{\Delta\phi}$ (region) = $I_{SD}$ (region, $\phi = 0°$) - $I_{SD}$ (region, $\phi = 90°$). $I_{SD}$ is SBS from all scatterers in each region and $I_{\Delta\phi}$ is SBS from large scatterers in each region.

We test the imaging system using 10μm spheres as in section 4.1. Figures 4.12a and 4.12b plot $I_{SD}$ ($\theta = 178°$, $\phi$) and $I_{\Delta\phi}$ ($\theta = 178°$) from two different regions. Note that since the sample does not have an underlying layer to provide multiple scattering and diffuse reflectance, $I_{SD}$ and $I_{\Delta\phi}$ do not evaluate the effectiveness of background removal. We also use Mie theory with the manufacturer's specifications to compute the expected $I_{SD}$ ($\theta = 178°$, $\phi$) and $I_{\Delta\phi}$ ($\theta = 178°$) spectra.

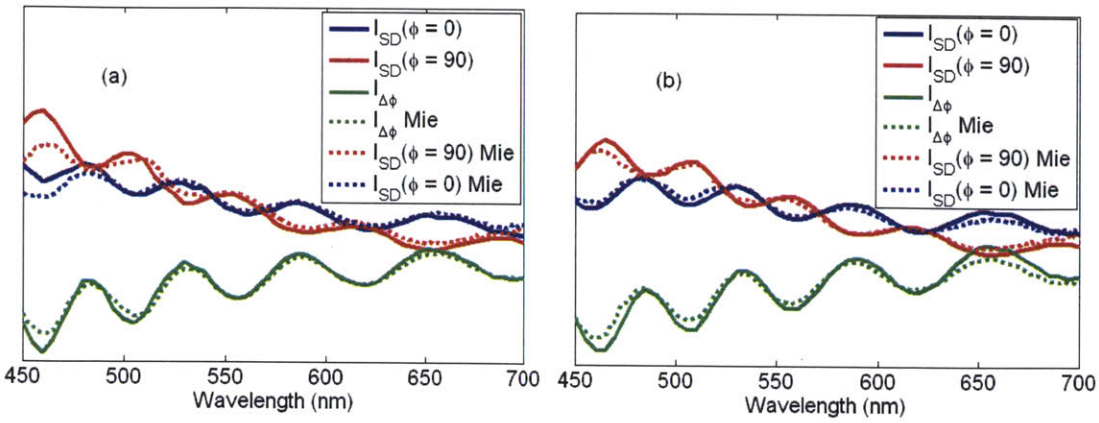


Figure 4.12: $I_{SD}(\phi)$ and $I_{\Delta\phi}$ measured from two regions (figures a and b). Mie theory predictions of $I_{SD}(\phi)$ and $I_{\Delta\phi}$. All spectra have been divided by their respective means for comparison.

Spectra measured from different regions of the sample agree with Mie theory predictions. This indicates the system is well calibrated and capable of mapping scatterer properties over a wide area. There are some deviations at shorter wavelengths. We believe this is due to our fixed value of $n_{glycerol} = 1.474$ at 589nm. As the wavelength deviates from 589nm, dispersion will cause greater errors in the modeling. Future studies will account for dispersion of glycerol.

SD/LSS and $\phi$/LSS work effectively together in wide area LSS imaging. We have calibrated an instrument capable of measuring SBS spectra from all scatterers in tissue and spectra specifically from large scatterers, mainly epithelial nuclei. The next step is to follow the experimental procedures of section 4.1 and 4.2. We will test the imaging system on more advanced tissue phantoms like those in figure 4.5 then advance to *ex vivo* tissue studies. Imaging results from many regions of a sample will be compared with those of the small area study in section 4.2.

[1] H. van de Hulst; Light Scattering by Small Particles; Dover Publications, Inc. (1981).

[2] D. Lide; CRC Handbook of Chemistry and Physics; CRC Press, LLC; 85th edition, (2004 - 05)

[3] R. Gurjar, V. Backman, L. Perelman, I. Georgakoudi, K. Badizadegan, I. Itzkan, R. Dasari, M. Feld; "Imaging human epithelial properties with polarized light-scattering spectroscopy"; Nature Medicine; Vol. 7, No. 11, 1245-48 (2001).

[4] V. Backman, M. Wallace, L. Perelman, J. Arendt, R. Gurjar, M. Müller, Q. Zhang, G. Zonios, E. Kline, T. McGillican, S. Shapshay, T. Valdez, K. Badizadegan, J. Crawford, M. Fitzmaurice, S. Kabani, H. Levin, M. Seiler, R. Dasari, I. Itzkan, J. Van Dam, M. Feld; "Detection of Preinvasive Cancer Cells"; Nature; Vol. 406, 35-6 (2000).

[5] J. Mourant, J. Freyer, A. Hielscher, A. Eick, D. Shen, T. Johnson; "Mechanisms of light scattering from biological cells relevant to noninvasive optical-tissue diagnostics"; Applied Optics; Vol. 37, No. 16, 3586-93 (1998).

[6] V. Backman, R. Gurjar, K. Badizadegan, I. Itzkan, R. Dasari, L. Perelman, M. Feld; "Polarized Light Scattering Spectroscopy for Quantitative Measurement of Epithelial Cellular Structures In Situ"; IEEE Journal of Selected Topics in Quantum Electronics; Vol. 5, No. 4, 1019-26 (1999).

[7] T. Farrell, M. Patterson, B. Wilson, "A diffusion theory model of spatially resolved, stead-state diffuse reflectance for the non-invasive determination of tissue optical properties"; Med. Phys.; Vol. 19, 879-88 (1992).

[8] G. Zonios, L. Perelman, V. Backman, R. Manoharan, M. Fitzmaurice, J. Van Dam, M. Feld; "Diffuse reflectance spectroscopy of human adenomatous colon polyps *in vivo*"; Applied Optics, Vol. 38, No. 31, 6628-37 (1999).

## Conclusion

Current surveillance procedures are incapable of detecting the subcellular biochemical and structural changes characteristic of cancer in its earliest stages. As a result, biopsies are conducted to sample a few areas of the tissue surface. Biopsies are expensive, painful, and only able to sample a small portion of the at risk area. Spectroscopic diagnosis is sensitive to biochemical and structural changes at the subcellular level and offers a potentially more efficient and accurate means of diagnosing cancer. Light scattering spectroscopy (LSS), in particular, has been demonstrated effective for detecting structural changes in epithelial cells. LSS relies on single backscattering (SBS) from epithelial cell structure. Previous researchers have developed techniques, such as polarization LSS (P/LSS), to isolate the single backscattering signal from a spectrum dominated by multiple scattering and diffuse reflectance. P/LSS is able to identify single backscattering, but it does not remove all of the multiple scattering signal.

This thesis has developed two novel differential LSS measurements for identifying the SBS signal. Space differential LSS (SD/LSS) uses patterned illumination where some regions of the tissue surface are illuminated and others are not. The difference between reflectance signals measured in illuminated and non-illuminated areas is SBS. $\phi$-angle differential LSS ($\phi$/LSS) measures reflectance at two azimuthal angles and their difference yields SBS specifically from large scatterers. $\phi$/LSS exploits the azimuthally asymmetric scattering of large particles.

This thesis strived to achieve several goals: 1) evaluate the potential of SD/LSS and $\phi$/LSS for measuring cellular morphology and diagnosing cancer; 2) develop a physical model based on light scattering theory to understand the origins of the measured spectra and to extract scatterer properties; and 3) develop instrumentation for conducting SD/LSS and $\phi$/LSS in wide area imaging. The goals have been achieved. 1) $\phi$/LSS has been validated on controlled tissue phantoms and results show scattering signatures from large scatterers are identified by the technique. The effectiveness of SD/LSS has been estimated with numerical simulations, which show smaller dark spots better isolate the SBS contribution to a reflectance spectrum. We have also used $\phi$/LSS to study SBS from *ex vivo* colon tissue. 2) We have developed a solution to the inverse scattering problem based on Mie theory and the single particle scattering assumptions. The results suggest that $\phi$/LSS identifies the longest dimension of epithelial nuclei in tissue. The results also show the scatterer size information extracted by $\phi$/LSS and the inversion procedure can diagnose cancer, but more studies are needed to determine sensitivity and specificity. 3) SD/LSS and $\phi$/LSS have been implemented together in a LSS imaging instrument, which has been calibrated with precision spheres. The next step will be to test the instrument with more advanced tissue phantoms like those described in chapter 4 and *ex vivo* tissue samples.

There are several avenues for future research. The effectiveness of P/LSS, SD/LSS, and $\phi$/LSS will be estimated with Monte-Carlo simulations. This will help to determine the amount of multiple scattering residual left by each technique. We will also investigate the accuracy of the Mie theory and single particle scattering approximations.

Studies will be conducted to better understand how non-spherical shape and multiple particle scattering affect results based on our Mie theory and single particle assumptions. Instrumentation will be developed to conduct more *ex vivo* tissue studies to assess the effectiveness of SD/LSS and $\phi$/LSS for cancer detection in single point and wide area imaging modalities. The primary goal of this project is to develop a clinical imaging system capable of studying dysplasia in cervix *in vivo* and in real time. SD/LSS and $\phi$/LSS will play central roles in this instrument. This instrument will combine the use of LSS with other spectroscopic modalities such as diffuse reflectance spectroscopy and fluorescence spectroscopy for more accurate diagnosis. Later studies will advance to other body organs such as the oral cavity and gastrointestinal tract.

# Appendix A

## Mie fitting program for $\phi$/LSS *ex vivo* tissue study

```
clear all;

% load the Mie data tables
load Tables/Table_tissue_m1p02_1p1.mat
temp0 = table0;
temp90 = table90;
clear table0 table90

size_range = 1:2:500;
index_range = 5:13; % default: 5-13
table_w = 11:61;
load Data\Cancer1_fit % load the ex vivo tissue data
[x,y] = size(exp0);
if (y == 51)
    data_w = 1:51;
elseif (y == 61)
    data_w = 11:61;
end
clear x y

sizes = sizes(size_range);

% collapse angles and wavelengths into 1D
angle = 1;
wavelengths = table_w;
C0 = squeeze(temp0(:,size_range,angle,wavelengths));
C90 = squeeze(temp90(:,size_range,angle,wavelengths));
C = C0-C90;
clear temp0 temp90
lamdas = lamdas(table_w);

% experimental data
angle1 = 36;
angle2 = 10;
wavelengths = data_w;
data0 = exp0(:,wavelengths);
data90 = exp90(:,wavelengths);
data = data0-data90;
data1 = data(angle1,:);
data2 = data(angle2,:);
clear data

DC1 = mean(data1);
DC2 = mean(data2);
frac_DC = 0.05;
frac_amp = 0.5;
AP_DC = frac_DC*abs(DC1-DC2);
data1 = data1 - DC1;
data = data1;
data2 = data2 - DC2;
data1 = smooth(data1,4);
data2 = smooth(data2,4);
AP_amp = frac_amp*(1-frac_DC)/51*sqrt(sum((data1-data2).^2));
Ddata1 = diff(data1);
Ddata2 = diff(data2);
AP_slope = (1-frac_amp)*(1-frac_DC)/51*sqrt(sum((Ddata1-
Ddata2).^2));
```

```
AP = AP_DC + AP_amp + AP_slope; %AP parameter
% select size range depending on AP parameter
if (AP > 4*10^-3) %cancer
    mean_range = 90:235;
else %normal
    mean_range = 50:110;
end

DP = 1/51*sqrt(sum(data.^2));
mag_data = data0(angle1,:)';
amp_data = sum(abs(data));
data = data'/amp_data;

LSE = Inf*ones(length(index_range),length(mean_range));
min0 = Inf;
count = 0;
for index = index_range
    count = count + 1;

    diam = 0;
for mid = mean_range
    diam = diam + 1;

for frac = 0.05:0.01:0.1
    stdev = roundn(frac*sizes(mid),-1);

    N1 = normpdf(sizes,sizes(mid),stdev);
    N = N1/sum(N1);

    fit = squeeze(C(index,:,:))'*N';
    fit = fit - mean(fit);
    amp_fit = sum(abs(fit));
    fit = fit/amp_fit;

    error = sum((fit-data).^2);

    ratio = amp_data/amp_fit;
    number = ratio/.0913*160000; % number of backscatterers N
    dmean = sizes(mid) + 0.2*stdev;
    cover = number/160000*.1*(dmean^2)/100; % CA

    if (cover < 0.1) || (cover > 2) %coverage area constraint
        continue;
    end

    mag_fit = ratio*squeeze(C0(index,:,:))'*N';

    K = 2;
    if max(mag_fit > K*mag_data) %reflectance constraint
        continue;
    end

    LSE(count,diam) = error;

    if (error < min0)
        index_opt = index;
        d_opt = mid;
        min0 = error;
        count_opt = count;
        diam_opt = diam;
    end
end
end
end
```

```
% ************************************
% extra outputs and plotting

min_std = Inf;
widths = 0.1:0.1:3;
LSE_std = Inf*ones(length(widths),1);
count1 = 0;
for stdev = widths
    count1 = count1 + 1;

    N1 = normpdf(sizes,sizes(d_opt),stdev);
    N = N1/sum(N1);

    fit = squeeze(C(index_opt,:,:))'*N';
    fit = fit - mean(fit);
    amp_fit = sum(abs(fit));
    fit = fit/amp_fit;

    error = sum((fit-data).^2);

    ratio = amp_data/amp_fit;
    number = ratio/.0913*160000;
    dmean = sizes(d_opt) + 0.2*stdev;
    cover = number/160000*.1*(dmean^2)/100;

    if (cover < 0.1) || (cover > 2) %coverage area constraint
        continue;
    end

    mag_fit = ratio*squeeze(C0(index_opt,:,:))'*N';

    if max(mag_fit > 2*mag_data) %reflectance constraint
        continue;
    end

    LSE_std(count1) = error;

    if (error < min_std)
        min_std = error;
        count1_opt = count1;
        std_opt = stdev;
        phi0_opt = mag_fit;
        LSE_opt = error;
        N_opt = number;
        CA_opt = cover;
    end
end

% figure
% mesh(sizes(mean_range),indices(index_range),LSE)

% figure
% plot(widths,LSE_std)

Nfit = normpdf(sizes,sizes(d_opt),std_opt);
Nfit = Nfit/sum(Nfit);
best_fit = squeeze(C(index_opt,:,:))'*Nfit';
best_fit = best_fit - mean(best_fit);
amp_fit = sum(abs(best_fit));
best_fit = best_fit/amp_fit;

% figure
% plot(exp0(angle1,data_w)-exp90(angle1,data_w))
```

```
% hold
% plot(exp0(angle2,data_w)-exp90(angle2,data_w),'r')

% figure
% plot(lamdas,exp0(angle1,data_w)-exp90(angle1,data_w),'b')
% hold
% plot(lamdas,best_fit*amp_data+DC1,'b:')

% DP
AP
% diameter = sizes(d_opt)
% width = std_opt
% m = indices(index_opt)
% error = LSE_opt
% CA_opt
% N_opt

% save Data\SearchGrid count_opt diam_opt count1_opt LSE LSE_std

% uncertainty
```

## Appendix B

## Signal to noise analysis

In this section we conduct a signal to noise analysis on the spectra measured from *ex vivo* colon tissue in section 4.2 to insure the signals are sufficiently beyond random noise. The signal, S, is the number of useful photoelectrons* falling on a region of the CCD during data acquisition. By useful, we mean the photoelectrons that contribute to the final signal of interest, which is the $\phi$/LSS spectrum. In the instrument of figure 4.1, noise comes from several sources. There is noise from room light and other sources of stray light. In this analysis, we assume these are adequately accounted for by the neutral density filter measurements. Other sources of noise originate at the CCD. The first, shot noise, is due to random arrival of photons and varies as $\sqrt{S_0}$, where $S_0$ is the total number of photoelectrons generated during each CCD exposure. Another significant type of noise, read noise, is uncertainty associated with transforming photoelectrons into a reading and is CCD dependent.

The signal to noise ratio S/N is defined as the number of useful photoelectrons divided by magnitude of noise in photoelectrons:

$$S/N = S / \sigma_{noise}$$

The total noise $\sigma_{noise} = \sqrt{\sigma_{shot}^2 + \sigma_{read}^2}$ is the Euclidean norm of all noises. For our CoolSNAP CCD, the read noise is approximately 6 photoelectrons / read / pixel. In our experiments, we obtain approximately $S_0 \approx 2000$ photoelectrons / read / pixel, so the shot

* Photoelectrons are generated by the CCD when light photons hit the chip. These are then read by the CCD to form the reading discussed in section 4.1.

noise is approximately 44.7 photoelectrons / read / pixel. Since we only read once per measurement, our instrument is shot noise limited. The signal to noise ratio can be rewritten as:

$$S/N \approx S / (S_o)^{1/2}$$

The S/N above is the signal to noise ratio for data from one pixel. As we mentioned in section 4.1, each reflectance spectrum is the result of binning 5000 pixels. Therefore, $S/N = (5000)^{1/2}\ S / (S_o)^{1/2} = 71\ S / (S_o)^{1/2}$. In our data, $S \approx 5$ photoelectrons / pixel for the weakest readings. As a result, S/N for each of the reflectance spectra $R_{\phi=0}$ and $R_{\phi=90}$ is approximately 8. S/N of the $\phi$/LSS spectrum is 0.71 * 8 = 5.6 because there is an equal amount of shot noise in the two reflectance spectra. S/N = 5.6 is sufficiently reliable.

## Appendix C

## Measuring scattering at select $\theta$ and $\phi$

The systems of figures 4.1 and 4.11 selectively measure reflectance at different scattering ($\theta$) and azimuthal ($\phi$) angles. In this section we illustrate how lenses and apertures are used to select the angular range of light from the sample permitted to pass to the CCD. Figure C.1 shows a light ray from a point on the sample incident on a lens placed one focal length away. The fourier plane is one focal length behind the lens.

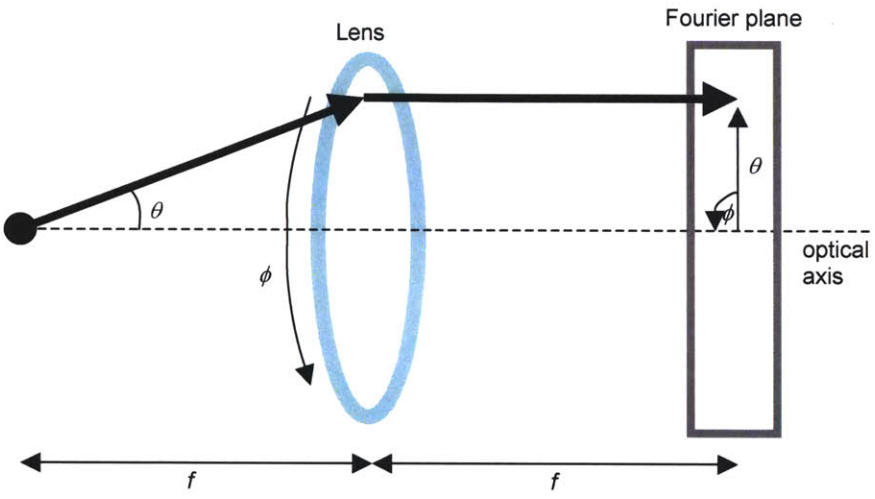


Figure C.1: Schematic of scattering and azimuthal angle separation on the fourier plane of a lens.

With this configuration, the scattering angle $\theta$ (from backscattering) is the angle between the ray and the optical axis. On the fourier plane, $f$*tan$\theta$ is the distance from the optical axis to the point the light ray is incident on the aperture. $\phi$ is the polar angle on the fourier plane. $\phi = 0°$ depends on the polarization direction of the illumination light. In the system of figure 4.1, the fourier plane is imaged onto the CCD. In the system of figure 4.11, an aperture is placed at the fourier plane to selectively pass certain $\theta$ and $\phi$.